Available online at www.sciencedirect.com
SCIENCE DIRECT®
Coordination Chemistry Reviews 249 (2005) 65–95
COORDINATION CHEMISTRY REVIEWS
www.elsevier.com/locate/ccr

Review

High resolution 1s core hole X-ray spectroscopy in 3d transition metal complexes—electronic and structural information

Pieter Glatzel [a,*], Uwe Bergmann [b,*]

[a] *Department of Inorganic Chemistry and CatalysisxDebye Institute, Utrecht University, Sorbonnelaan 16, 3584 CA Utrecht, The Netherlands*
[b] *Stanford Synchrotron Radiation Laboratory, P.O. Box 20450, Stanford, CA 94309, USA*

Received 22 July 2003; accepted 20 April 2004
Available online 26 June 2004

Contents

Abstract

The creation of a 1s core hole in a 3d transition metal ion gives rise to an emission spectrum that can be recorded using a crystal analyzer. K shell X-ray spectroscopy using an analyser energy bandwidth of ~1 eV is sensitive to electron–electron interactions and orbital splittings and

* Corresponding author.
E-mail addresses: pieter.glatzel@gmx.org (P. Glatzel), bergmann@slac.stanford.edu (U. Bergmann).

doi:10.1016/j.ccr.2004.04.011

preserves the advantages of the hard X-ray probe. We review recent developments in Kα and Kβ spectroscopy and show how the chemical sensitivity of the fluorescence lines can be exploited for selective X-ray absorption studies. When the photo excitation energy is tuned close to the K edge threshold, the phenomenon known as X-ray resonant Raman or resonant inelastic X-ray scattering (RIXS) occurs. RIXS spectroscopy on 3d transition metals at the 1s resonances with lowest incident energies (K pre-edge) is a very recent technique. We discuss basic aspects and demonstrate with several examples its potential as a future routine spectroscopic tool.

Keywords: X-ray fluorescence; X-ray absorption; Resonant inelastic X-ray scattering; 3d Transition metal; Multiplet theory; Electronic structure; Chemical bonding

1. Introduction and overview

Inner-shell spectroscopies are applied to study 3d transition metal complexes because they are element specific and sensitive to the metal oxidation and spin state as well as the local geometry. The direct approach to probe the electronic structure of a transition metal ion in different chemical environments using X-rays is to take advantage of the dipole allowed 2p–3d transition. L-edge absorption spectroscopy with its pronounced chemical sensitivity is an established technique (see review article by de Groot in this volume). However, the L-edge energies of 3d transition metals lie below 1.1 keV (soft X-ray region) and many systems and/or sample conditions profit from the larger penetration depth of hard X-rays (Fig. 1). There are also cases, e.g. very photosensitive metalloproteins, where the problem of radiation damage favors the weaker interacting hard X-ray probe.

The 3d transition metal K-edges range from 4 to 10 keV and lie thus in the hard X-ray region. K-edge absorption spectroscopy on 3d transition metal compounds has become a routine tool in the study of these chemically important systems [2,3]. The extended X-ray absorption fine structure (EXAFS) is widely used to determine short-range geometry parameters of the metal site [4–6], and the near edge structure (XANES) provides information on metal oxidation state and coordination [7–11]. However, the XANES region is formed by numerous effects that mainly reflect the delocalized metal p density of unoccupied states. In order to obtain a more localized view of the electronic structure at the metal site it is desirable to use a hard X-ray technique that probes the lowest unoccupied orbitals, i.e. the metal 3d shell.

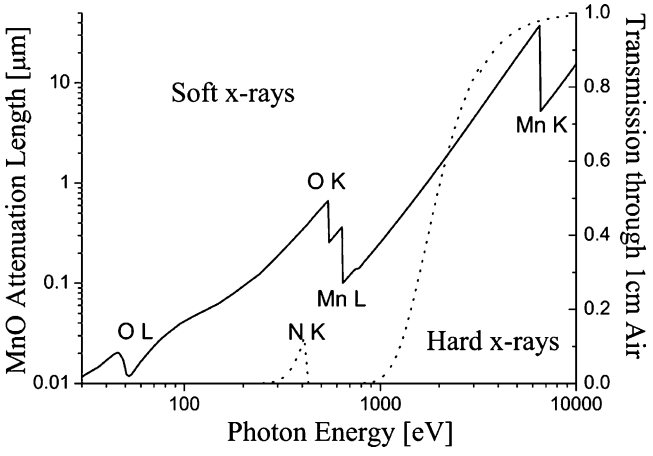

Fig. 1. X-ray attenuation length in MnO (solid) and transmission through 1 cm air at 760 Torr and RT (dotted) [1]. The large attenuation length makes hard X-ray spectroscopy a bulk sensitive probe. The high transmission through gases allows for experiments where the sample is kept in ambient conditions.

Selection rules for electronic transitions induced by interaction with a photon pose a serious obstacle in the study of the metal 3d shell if a 1s electron is excited in the spectroscopic process. The electric and magnetic field of the radiation can be generated from a vector potential $\vec{A}$. Using a plane wave description, $\vec{A}$ contains the function $\exp(i\vec{k}\vec{r})$ that can be expanded as

$$\exp(i\vec{k}\vec{r}) = 1 + i\vec{k}\vec{r} + \cdots \quad (1)$$

with propagation vector $\vec{k}$ and spatial coordinate vector $\vec{r}$. Carrying only the first term (unity) when treating the interaction of the electromagnetic field with an electron is the dipole approximation with the selection rule $\Delta l = \pm 1$ for the atomic orbital angular momentum, e.g. 1s–4p transitions. The second term accounts for electric quadrupole interactions with the selection rule $\Delta l = 0, \pm 2$, e.g. 1s–3d transitions (we neglect magnetic dipole radiation).[1] The quadrupole transition matrix elements are reduced compared to the dipole transition matrix elements by a factor on the order of the fine structure constant $\alpha \sim 1/137$ [12–14] and are therefore more difficult to observe in transition metal 1s spectroscopies.

In this article, we review two approaches to tackle the problem of gaining information on the 3d shell without losing the advantage of the hard X-ray probe. First, we can restrict ourselves to dipole allowed transitions by looking at the 2p or 3p–1s K fluorescence lines that are emitted after 1s core hole creation. In this case, we have to derive the information about the metal 3d shell indirectly by analyzing the interactions between the 2p or 3p hole and the 3d electrons. These interactions are considerable because of the large overlap between the 2p (3p) and the 3d wave functions [15]. The K fluorescence lines therefore show a pronounced chemical sensitivity. The chemical information obtained in Kα and Kβ main line fluorescence spectroscopy

[1] The selection rules for non-vanishing transition matrix elements in point group symmetries with the metal ion embedded in a ligand environment are discussed in Section 7.1.2.

mainly concerns the metal ion spin state. There is a considerable number of publications on this topic, many of them dealing with fundamental aspects of the theoretical interpretation. We will review recent new insights and applications in inorganic (bio)chemistry.

Fluorescence transitions from orbitals higher than the metal 3p shell (Kβ satellite lines) mainly arise from metal and ligand electrons that contribute to the metal p density of occupied states. The energy position of one of the spectral features, the 'cross-over' peak, indicates the type of ligand that is coordinated to the metal ion. Furthermore, using the angular dependence in the fluorescence emission of a single crystal it is possible to derive the symmetry and thus the spatial distribution of an occupied molecular orbital.

The other approach is to study the weak K absorption pre-edge structure, thus directly probing 1s–3d transitions. (For simplicity, we refer to the pre-edge as '1s–3d' transitions and discuss p–d hybridization in Section 8.1). The dipole allowed transitions that form the K main edge at higher energies, however, cause a strong background in the range of the pre-edge structure. A detailed analysis of the K pre-edge spectral features in conventional absorption spectroscopy is therefore often limited and connected with a rather large uncertainty. We will show that resonant inelastic X-ray scattering (RIXS) spectroscopy can be used to circumvent this problem and to furthermore gain additional information. In RIXS spectroscopy, a second energy axis—the energy transfer or final state energy—is added to that of the incident photon. This enables a separation of the pre-edge structure from the main K absorption edge along the incident energy axis. Furthermore, the electronic states along the additional energy transfer axis correspond to the final states in soft X-ray L-edge and M-edge spectroscopy. Even though the spectral shapes along the energy transfer do not necessarily coincide with the spectra as obtained in the soft X-ray experiment, they still bear information on the metal ion electronic structure that is complementary to K-edge absorption. RIXS spectroscopy at the transition metal K pre-edges is a very recent technique that benefits from intense third generation storage ring facilities and advances in X-ray analyzer instrumentation. Its full potential is not yet developed, and we hope this review of the current status will help to stimulate such progress.

We note that emission and RIXS spectroscopy using hard X-rays can also be performed on rare earths. Here, the L-edges lie in the hard X-ray range and some studies exist [16–18].

2. K shell fluorescence lines

The photons that are emitted after creation of a hole in the 1s shell form the K fluorescence emission spectrum (Figs. 2 and 3). The strongest K fluorescence lines result from 2p to 1s transitions (Kα lines). Approximately eight times weaker are the 3p–1s transitions and 50–100 times weaker are transitions to the 1s shell from higher orbitals [19]. Both latter fluorescence emissions are denoted Kβ lines. We will refer to the electronic state with a 1s core hole as the *intermediate state*. The Kα and Kβ *final states* are reached when the 1s vacancy is filled.

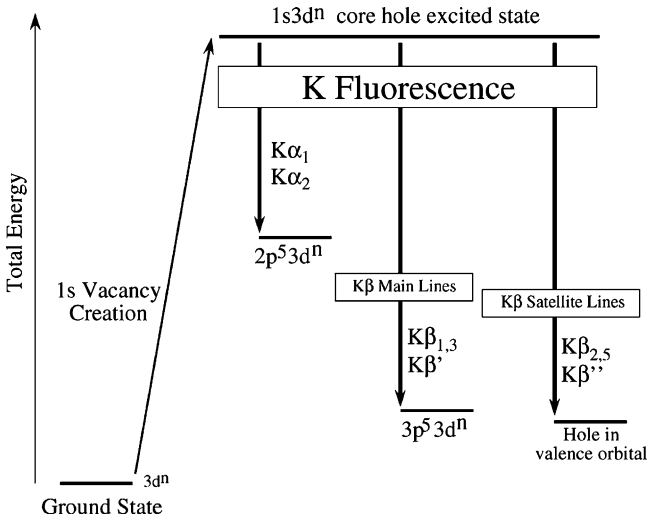

Fig. 2. Simplified energy scheme for K fluorescence emission. The different radiative decay channels of the 1s vacancy give rise to the K fluorescence spectrum. The continuum electron that occurs after 1s photoionization is neglected in the intermediate and final states. Atomic configurations are used for simplicity.

In an experimental setup that employs a solid state detector to record the K fluorescence emission (e.g. for Ge the resolving power is $E/\Delta E \sim 40$) the Kα and Kβ groups can be separated from each other but no fine structure can be resolved. The intensity ratio I(Kβ)/I(Kα) has been used to determine the electron occupancy in 3d transition metals

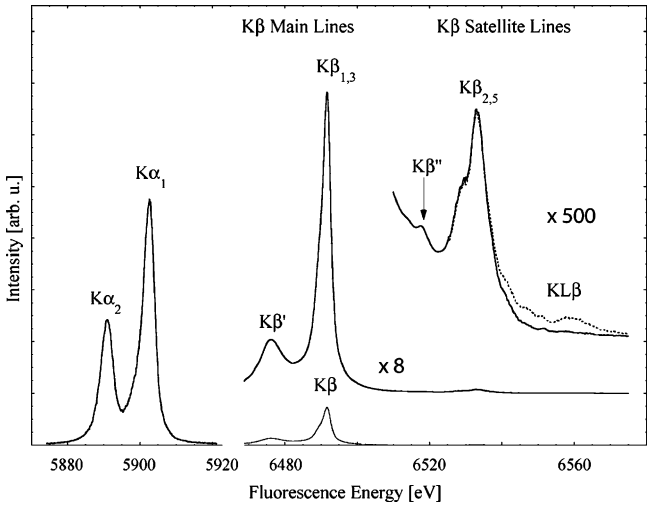

Fig. 3. K shell emission lines in MnO. The final state configurations are given in Fig. 2. The Kβ satellite lines are shown for excitation energies below and above the KL edge, where a 2p electron is excited together with a 1s electron (multiple electron excitation) [24]. The KLβ structure (dotted line) thus arises from doubly ionised final states. The magnification factors for the Kβ main and satellite spectra are given.

[20,21]. The differences in $I(K\beta)/I(K\alpha)$ are, however, small and an accurate fitting procedure is required in order to obtain reliable numbers for the ratio. In a recent study by Sakurai and Eba using a 'downsized' Johann-type spectrometer with medium energy resolution ($E/\Delta E \sim 600$) the normalized $K\beta'$ and $K\beta_{2,5}$ intensities were found to be suitable for chemical classification (cf. Fig. 3) [22]. We note that superconducting tunnel junction detectors as they are developed by e.g. Friedrich et al. [23]. are capable of a similar medium energy resolution in the keV photon energy range.

In order to be able to separate spectral features within the Kα and Kβ groups and detect changes of the spectral shape due to the chemical environment it is necessary to achieve a resolving power of order $E/\Delta E > 5000$, which currently can only be obtained with a spectrometer based on perfect-crystal Bragg optics. In this review, we focus on the interpretation and application of such high resolution fluorescence spectra.

The nomenclature of the Kβ spectral features used in Fig. 3 has its origin in the spectroscopy of high Z materials, such as rhodium and uranium, where the 3p spin–orbit splitting is large enough to yield two distinct $3p_{1/2}$ ($K\beta_3$) and $3p_{3/2}$ ($K\beta_1$) final states [25,26]. $K\beta_2$ was assigned to transitions from 4p orbitals and $K\beta_5$ from 3d orbitals. The nomenclature was transferred to transition metals and there, with a deeper understanding of the dominating interactions, partly lost its actual physical meaning. We will call 3p–1s transitions Kβ main lines and transitions at higher fluorescence energies Kβ satellites. The Kβ structure at highest fluorescence energies (KLβ) is due to double ionizations that are not discussed here [24,27]. The origins of the line splittings in transition metal fluorescence emission are discussed in Section 5.

2.1. Modes of 1s core hole creation

We show K fluorescence spectra where the 1s hole is created in two different ways (modes of excitation). In photoionization, a photon excites a 1s electron into the continuum. Alternatively, one can take advantage of radioactive electron capture decay. An orbital electron reacts with a proton in the nucleus yielding a neutron that remains in the nucleus and an escaping electron neutrino [28]. The atomic number of the daughter nucleus is decreased by one while the atomic mass number is unchanged: $Z^A + e^- \rightarrow (Z-1)^A + \nu_e$. The capture rate depends on the probability of finding the electron inside the nucleus and is therefore largest for 1s electrons (K capture decay). Fig. 4 illustrates for radioactive ^{55}Fe and stable ^{54}Mn that the same formal atomic configurations are reached after K capture in ^{55}Fe and 1s photoionization in ^{54}Mn, respectively. The fluorescence energies of the ^{55}Fe K capture emission correspond to the Mn spectrum after photoionization. This suggests a comparison of the X-ray fluorescence following the two modes of excitation. We note that the influence of nuclear recoil and other nuclear effects (nuclear excitation, isotope effect) can be neglected for the fluorescence emission in ^{55}Fe [29,30].

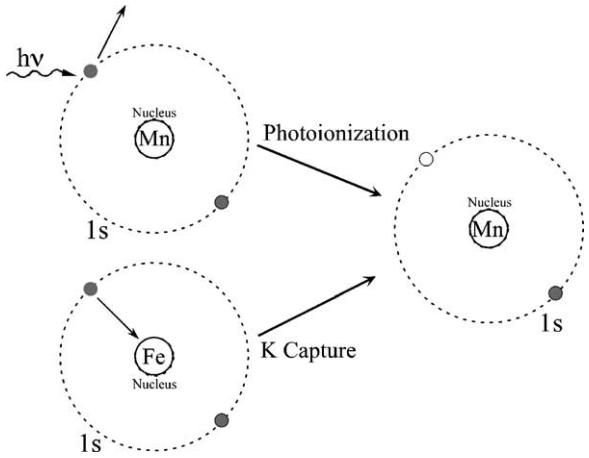

Fig. 4. K capture in ^{55}Fe and 1s photoionization in Mn. Both processes result in an ion that has a Mn ($Z = 25$) nucleus and a hole in the 1s shell.

3. Theories

The analysis of inner-shell spectra in a free transition metal atom or ion is a complex many-body problem that cannot be solved analytically and numerical simulations are limited by computer capacities. Thus, approximations have to be made and it remains a topic of controversy what effects should be included in the theoretical model [31]. The matter becomes even more complicated when the atom is embedded in a ligand environment [32–34]. Transition metal systems can be divided into two groups: Bulk materials with a pronounced band structure formation and molecular coordination complexes. Many authors treat even the former by means of a cluster model (e.g. MX_6 in octahedral symmetry with metal M and ligand X) and either neglect band formation at all or introduce it empirically.

The choice of theory depends on the electron transition that is observed experimentally. K-edge absorption spectra above the pre-edge can be well reproduced within a multiple scattering formalism based on real space Green functions ('FEFF code') [10]. This code, however, does not fully account for intra-atomic electron–electron interactions that lead to a multiplet structure of the electronic energy levels. Electronic transitions that involve resonant excitations and/or p core orbitals in the intermediate and final state are usually better modeled by theoretical approaches that are based on atomic multiplet theory [15,35]. In order to account for the ligand environment, the spherical (SO_3) symmetry of the wavefunctions in the atom is reduced to the local point group symmetry (e.g. octahedral, O_h) of the metal ion in the compound. Group theoretical considerations then allow to determine the orbital splitting (qualitatively, e.g. 3d to t_2 and e in cubic symmetry), wavefunction mixing and electron transition selection rules.

In crystal field theory the ligands are represented as point charges and a purely ionic system is considered. Ligand field theory includes covalency (orbital hybridization) and thus gives a more realistic picture of the electron configuration. The ligand field multiplet approach to analyze inner-shell X-ray spectra of transition metal compounds already suggested in 1959 by Tsutsumi and further developed by Sugano, Thole and others has been applied successfully to L-edges and K fluorescence spectra (see review by de Groot in the present volume). The multiplet interpretation for the overall structure of K fluorescence spectra is also supported by results obtained using photoelectron spectroscopy (2p and 3p XPS) in compounds and free metal atoms [36–40].

Ligand field multiplet theory is a semi-empirical approach. Ligand field and hybridization parameters have to be obtained from experiment or ab initio calculations. Density–functional approaches are ab initio theories but at present do not account for multiplet structure. Some authors invoked density–functional theory for qualitative arguments to explain experimental observations in inner-shell spectra [41,42]. The simulation of inner-shell spectra using ab initio wavefunction-based (as opposed to density–functional based) molecular orbital theory is hampered by the fact that considerable computing powers are required. With improving computer resources this approach is very promising because it can potentially account for the full multiplet structure while the combination with molecular orbital theory ensures an accurate description of orbital hybridization [43].

In this review we show theoretical spectra that were obtained using ligand field multiplet theory to interpret Kα and Kβ main lines as well as the K absorption pre-edge structure in RIXS spectroscopy. Molecular orbital theory is used for the Kβ satellites. Here, the molecular orbitals were obtained from density–functional calculations as developed by Kohn and Sham [44,45].

3.1. The effective number of 3d electrons

Inorganic chemists generally group transition metal complexes in terms of the metal oxidation state. Inner-shell spectroscopists, on the other hand, find in many cases a different ordering, and the concept of oxidation state is only of limited merit when trying to explain the spectral shapes. This apparent disagreement arises from the attempt to derive the number of metal valence electrons from the oxidation state. Even though this might work rather well for very ionic compounds, it can generally not be applied to complexes that exhibit strongly covalent bonds and where the electron density for a valence orbital is spread across several atoms.

Inner-shell fluorescence spectroscopy tests the immediate surrounding of the excited ion because the Coulomb interaction between the core hole and the valence electrons is only appreciable within a short-range. The K absorption pre-edge structure that we study in transition metal RIXS spectroscopy arises from excitations into the lowest unoccupied orbitals that are mainly localized around the metal ion. Electron and spin densities on the excited ion do not correspond to the numbers derived from the oxidation state. In order to interpret the experimental results it is necessary to describe the electron configuration within a charge density or molecular orbital picture. To make the connection to multiplet theory we can expand the electron density or molecular orbitals in terms of atomic orbitals and determine their occupation by means of a population analysis. Already in 1955 Mulliken developed a method to extract the population of atomic orbitals in compounds [46]. More sophisticated procedures have been introduced recently [47–49]. We thus obtain an 'effective number' of 3d electrons $3d_{\mathrm{eff}}$, i.e. the number of electrons that can be assigned to the metal 3d shell [41,42,50]. The effective number of 3d electrons is divided into spin-up and spin-down and from the difference we obtain the net electron spin S_{3d}^{eff} on the metal ion. We then assume that the core hole primarily interacts with the metal 3d electrons and the interaction with the ligand valence electrons can be neglected. The effective number of 3d electrons is in most cases fractional.

4. Instrumentation

The central component of an emission spectrometer is a Bragg crystal that spectrally analyzes the fluorescence from the sample and reflects it onto a photon detector. Several experimental setups have been conceived over the decades [51–53]. We use a spherically bent Johann type crystal in a one-to-one focusing Rowland geometry in connection with a solid state detector [54–56]. In order to enlarge the solid angle of collection the number of analyzer crystals in our setup can be increased up to eight crystals, all aligned on Rowland circles that intersect at the two focal points (Fig. 5). Both K capture and photoexcitation experiments have identical setups in terms of analyzers and detector. The source point of the K capture experiment corresponds to the X-ray beam spot on the sample in the photoexcitation setup. The X-ray beam in the photoexcitation experiment can be produced either with an X-ray tube or in an electron/positron storage ring that generates synchrotron radiation. Synchrotron radiation experiments have the advantage of much larger X-ray intensity and full tunability of the incident X-ray energy and polarization. Typical storage ring based experiments have thus two X-ray optical elements—a monochromator to choose the energy of the incident X-rays and an analyzer to choose the energy of the fluorescence emission spectrum. Good energy resolution in the incident X-rays gives the possibility to combine conventional absorption and emission spectroscopy as it is done in selective EXAFS and RIXS spectroscopy.

The simplified schematics of a storage ring based setup with four analyzer crystals is shown in Fig. 5. The incident X-ray beam is guarded by an aperture slit to define the source size and the photon flux is recorded using an ion chamber. Two more ion chambers with a calibration standard can be

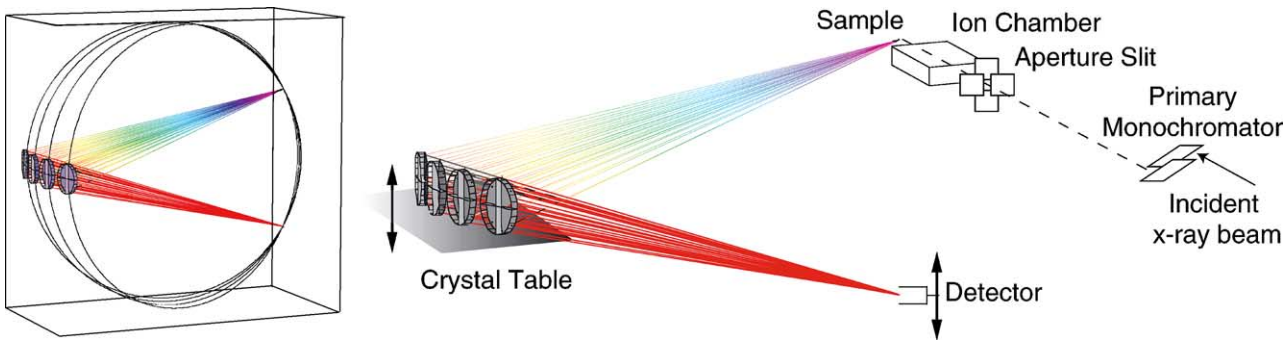

Fig. 5. Experimental set up at a storage ring beamline. The arrows indicate the motion of the components when a spectrum of the emitted X-rays is taken. The inset shows the orientation of the Rowland circles for the four analyzer crystals.

added downstream of the sample to record absorption scans of the sample in transmission mode and to correct for energy drifts in the primary monochromator, respectively.

The multi-crystal spectrometer described here was specifically designed for applications in inorganic (bio)chemistry, where systems can be very dilute and/or fluorescence features might be weak. It thus covers a large solid angle of collection and its simplified scanning procedure ensures good stability to avoid energy drifts. Kβ fluorescence studies of dilute samples such as metalloproteins have been performed at second generation synchrotron radiation sources (incident flux I_0 of order some 10^{11} photons/s) [57,58], but a more intense third generation source ($I_0 \sim 10^{13}$ photons/s) was used in recent site-selective EXAFS and RIXS studies [59–61]. In fact, most third generation storage rings have active R&D programs to pursue novel instrumentation for these evolving techniques (e.g. ESRF: ID-16 and ID-26, APS: Sector 3, Spring8: Bl 12XU, PETRA III, SOLEIL, DIAMOND: inelastic scattering beamlines). Active development for novel instrumentation is also pursued at first (CHESS, HASYLAB) and second (NSLS, DELTA) generation synchrotron radiation facilities.

We note that the experimental conditions with respect to sample environment in transition metal K fluorescence and RIXS spectroscopy using hard X-rays are identical to conventional K-edge XANES and EXAFS spectroscopy. Radiation sensitive samples can be cooled down below 10 K and kept in an exchange gas environment. Radiation damage studies can be accurately performed. The use of hard X-rays gives considerable experimental freedom and for future studies one can envision for example in situ studies (e.g. 'operando', photolysis) or simultaneous control (e.g. FT-IR, optical Raman) measurements.

5. Chemical sensitivity of the Kα and Kβ main fluorescence lines

As soon as K emission spectra were recorded with the high resolution of a crystal analyzer, it was found that the features show a pronounced chemical sensitivity [26,62–64]. In the Kα and the Kβ main lines, spectral changes depending on the chemical environment arise predominantly from the exchange interaction between the core hole (2p or 3p) and the net electron spin in the metal valence shell, i.e. the effective number of unpaired metal 3d electrons. Spectral changes with the metal spin state are, however, very different between Kα and Kβ lines because the magnitudes of the electron–electron interactions (Slater integrals) and spin–orbit coupling depend on the type of core hole.

As an example, we compare in Table 1 the values for Mn in a $2p^53d^5$ (Kα final states) and a $3p^53d^5$ (Kβ main final states) configuration. The spin–orbit splitting ζ_p is almost ten times larger for a 2p hole in the final state while the exchange integrals G_{pd} are about three times larger for a 3p hole. As a consequence, the overall spectral shape of Kβ main line emission is dominated by the (3p,3d) exchange interaction while the Kα spectra are shaped by the 2p spin–orbit splitting.

The same final states as in K fluorescence spectroscopy can be reached in inner-shell photoelectron spectroscopy (XPS or ESCA) which is a well-studied field [37]. A detailed analysis of the 2p XPS final states—that correspond to the Kα final states—in atomic Mn is discussed by e.g. Wernet et al. [65]. Here, the authors discuss the accuracy of the *jj*-coupling scheme to describe the final states with a 2p hole. A general discussion of 2p XPS in transition metal compounds is given by Parlebas [66]. A comparison between 2p XPS and Kα emission for Mn oxides and Fe cyanides is discussed by Oku et al. [67]. Likewise, the final states of 3p XPS correspond to the Kβ final states. They are discussed

Table 1
Slater integrals and spin–orbit parameters (eV) for a Mn^{2+} ion with the given core hole electron configurations

	$2p^53d^5$	$3p^53d^5$
ζ_d	0.06	0.05
ζ_p	6.85	0.80
F^2_{dd}	12.21	11.47
F^4_{dd}	7.65	7.18
F^2_{pd}	6.99	12.40
G^1_{pd}	5.18	15.40
G^3_{pd}	2.85	9.38

by e.g. Borne et al. [68] in particular the term dependent life time broadening in context with symmetry mixing of the final states.

In the following, we show Kα and Kβ results in Mn and Fe compounds where the effective number of unpaired 3d electrons can be estimated from the metal oxidation and spin state. We then demonstrate some cases where this model breaks down. Ligand field multiplet calculations are presented that simulate the experimental spectra.

5.1. Kβ lines

Fig. 6 shows the Kβ main lines in Fe_2O_3, $K_3Fe(CN)_6$ and $K_4Fe(CN)_6$ following K capture decay. The nominal spin states of the three compounds are $S = 5/2$, 1/2 and 0, respectively, thus spanning the whole range from the largest to the smallest possible spin state in a transition metal compound. There are two prominent features in the Fe_2O_3 spectrum. At high fluorescence energies is the strong $K\beta_{1,3}$ line. The peak is slightly asymmetric with a weak shoulder on the low energy side. The shoulder arises from a spin flip in the metal valence shell [30,69]. This is a many-electron effect and shows the correlation in the electronic shell; upon the 3p–1s transition of one electron, a second electron in the 3d shell responds to the change of electronic configuration by changing its spin orientation relative to the other valence electrons.

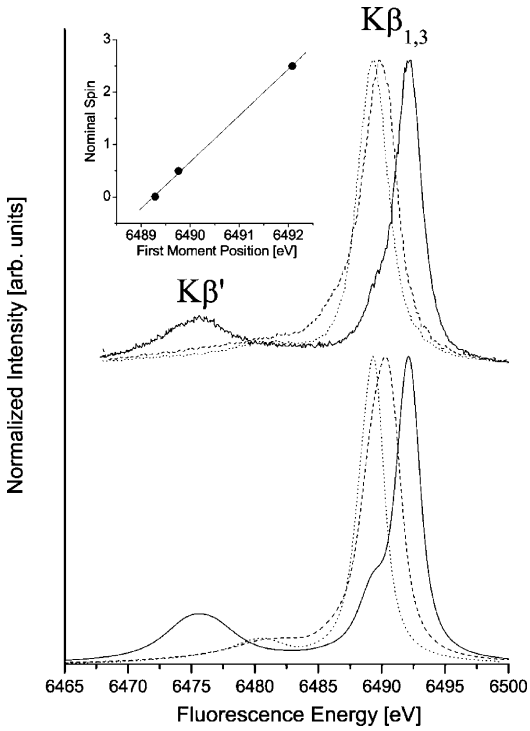

Fig. 6. (top) Kβ fluorescence lines in $^{55}Fe_2O_3$ (solid line), $K_3{}^{55}Fe(CN)_6$ (dashed line) and $K_4{}^{55}Fe(CN)_6$ (dotted line) measured after K capture decay. The inset shows the nominal valence spin state vs. the $K\beta_{1,3}$ first moment position with a linear fit. Ligand field multiplet simulations for the three compounds (bottom).

The Kβ′ feature in Fe_2O_3 at lower fluorescence energies is due to the (3p,3d) exchange interaction. It has also been assigned to either collective (plasmon) excitations or charge-transfer processes [70,71]. Photoemission spectroscopy on free atoms, however, shows that intra-atomic interactions dominate the Kβ spectral shape [40,68]. Kβ′ and $K\beta_{1,3}$ line move towards each other with decreasing valence spin and thus smaller (3p,3d) exchange interaction. The Kβ′ structure merges into other weak final states on the low energy side of the $K\beta_{1,3}$ line for $S = 0$. These states are due to many electron excitations where additional electrons undergo a t_{2g} to e_g transition (so called 'shake-up' transitions) while simultaneously a 3p electron decays into the 1s vacancy. The final states of these shake-up transitions have a spin-state $S > 0$ but are considerable weaker than the single-electron transitions.

The calculated spectra in Fig. 6 were obtained using multiplet theory with the ionic Fe species embedded in a ligand field. The calculations include the above mentioned many electron transitions. A linear increase of the final state lifetime was applied to the spectra to account for the term dependent lifetime broadening as discussed by Glatzel et al. [30] and Taguchi et al. [72]. For the cyanides, 10Dq was set to 5 eV in the calculations to yield a low-spin configuration in the valence shell. A cubic ligand field does not split the 3p orbitals. The exact value of 10Dq thus has little influence on the overall spectral shape as long as a low-spin (or high-spin) configuration is maintained [69]. The effect of a non-cubic ligand field on the Kβ main lines was studied in a single crystalline Mn nitrido complex [73].

The theoretical spectra reproduce the experimental results quite well [29]. The remarkable point about the calculations is that the $3p^5 3d^n$ final state energy, i.e. the center-of-gravity of the entire multiplet was set to equal values in all three calculations. With this assumption the relative energy positions of the $K\beta_{1,3}$ line are very well reproduced and we can conclude that the shift of the $K\beta_{1,3}$ line to lower energies is not caused by a change in nuclear screening between different oxidation states (here between $K_3Fe(CN)_6$ and $K_4Fe(CN)_6$) but almost entirely by variations in the exchange splitting.

Kβ spectroscopy is thus sensitive to the metal spin state. More exactly, it reflects the effective number of unpaired metal 3d electrons. This sensitivity was used for example to determine Mn oxidation in coordination complexes and photosystem II as well as in $Li_xMn_2O_4$ [57,58,69,74,75]. A study of Mn oxides was carried out by Quian et al. [76,77]. Badro and co-workers investigated the local spin moment in the high-pressure phases of various Fe compounds by means of Kβ spectroscopy [78–81]. However, they do not show their spectra on an emitted energy scale with correct relative energy calibration. Instead, the spectra were shifted in energy in order to align the $K\beta_{1,3}$ peaks and the Kβ′ peak intensity was used to derive the local spin. Alternatively, the spectra could be aligned with equal center-of-gravity energies of the entire spectral area. In this case our arguments concerning the $K\beta_{1,3}$ peak position apply.

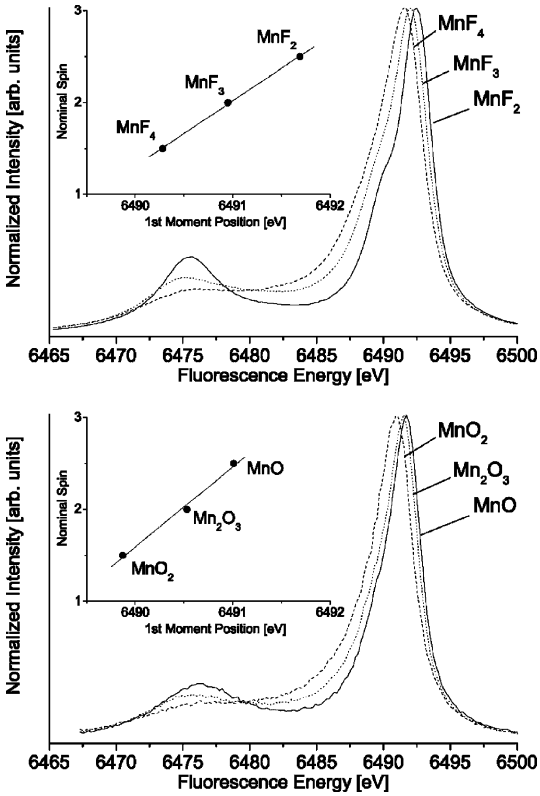

Fig. 7. Kβ lines (top) in the Mn fluorides MnF_2 (solid line), MnF_3 (dashed line) and MnF_4 (dotted line) and (bottom) Kβ lines in the Mn oxides MnO (solid line), Mn_2O_3 (dashed line) and MnO_2 (dotted line). The insets show the first moment positions of the $K\beta_{1,3}$ peak with a linear fit.

Using a few assumptions we can be more quantitative about the $K\beta_{1,3}$ chemical shift. If the valence shell orbital angular momentum is zero and spin–orbit interactions can be neglected we can use multiplet theory to find a linear relation between the exchange energy splitting and the spin in the metal 3d shell [29]. This is sometimes referred to as van Vleck's theorem [35,82]. The orbital angular momentum was indeed found to be zero in many transition metal compounds by studying the magnetic susceptibility [83]. A theoretical explanation of this so-called 'quenching' of the orbital angular momentum was provided again by Griffith and van Vleck [34,84]. Using the nominal spin state we can see in Fig. 6 that the $K\beta_{1,3}$ peak positions (defined as the first moment [58]) of the three Fe compounds lie indeed almost on a straight line.

Examples for Mn fluorides and oxides measured after photoionization are shown in Fig. 7. The spectra for a series of Mn coordination complexes was published by Peng et al. [69]. We see again pronounced shifts with the Mn oxidation and thus the spin state and the first moments approximately shift with the nominal spin state in a linear fashion. However, a different behavior between the fluoride and the oxide series can be observed and the absolute first moment positions for samples with equal oxidation states do not agree between

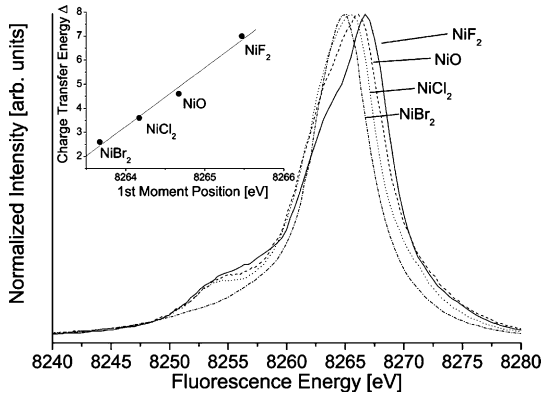

Fig. 8. Kβ lines in a series of Ni(II) compounds. The first moment positions are plotted vs. the charge transfer energy Δ in the inset.

the two series of compounds. The formal oxidation state is therefore not an appropriate quantity to explain the spectra.

We can illustrate the situation in an electron density picture by describing an electron cloud that becomes less localized and more distributed between the metal ion and its ligands for more covalent compounds. The short-range of the (3p,3d) exchange interaction makes the K fluorescence line only sensitive to the electron density localized on the metal ion, i.e. the effective number of unpaired 3d electrons. This effective spin state can no longer be derived from the oxidation state. The degree of covalency is connected via the effective number of unpaired 3d electrons to the magnitude of the exchange splitting. This observation holds for all transition metal compounds.

There are two ways in multiplet theory to treat covalency as discussed by de Groot [85]. First, one can scale down the Slater integrals that describe the exchange splitting to account for the smaller net electron spin on the metal ion. We will show in the next section where we discuss Kα emission, that the scaling factor can be obtained from density–functional calculations. The linear relation between exchange energy and number of 3d electrons can thus be retrieved. Secondly, one can introduce the charge transfer energy Δ that describes the energy that a ligand electron requires to hop to the metal ion. In a $3d^4$ configuration, for example, Δ determines (besides other parameters) how much of a $3d^5\underline{L}$ ($\underline{L}$ denoting a hole in a ligand orbital) configuration is admixed. The actual electronic state is a linear combination of both configurations and the effective number of 3d electrons is between 4 and 5.

Values for Δ were determined by van der Laan et al. for a series of Ni(II) compounds [86]. Corresponding Kβ spectra and a plot of the $K\beta_{1,3}$ peak position versus Δ are shown in Fig. 8. A monotonic relation between Δ and the $K\beta_{1,3}$ peak position is observed even though it is not strictly linear. This is because Δ does not behave linearly to the effective net spin on Ni. To obtain a number for $3d_{eff}$ and S^{3d}_{eff} a more exact theoretical treatment using configuration interaction calculations including three configurations would be necessary [87]. Alternatively density–functional calcula-

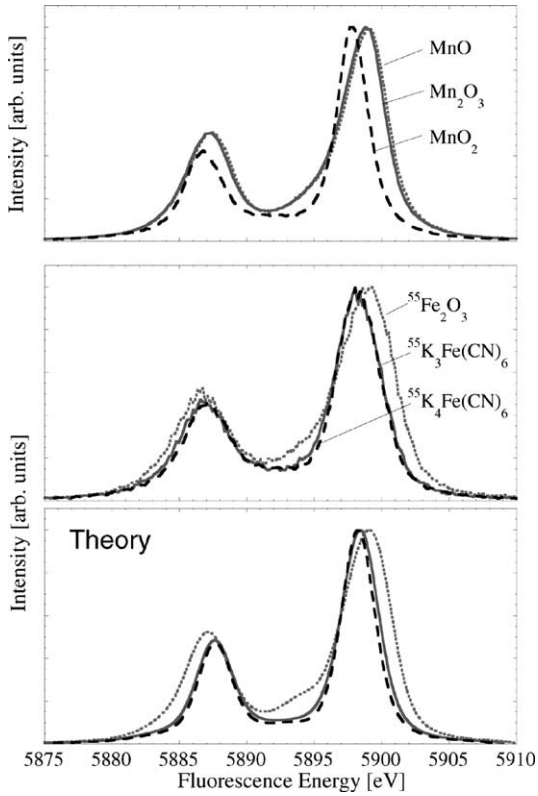

Fig. 9. Kα lines in a series of Mn and ^{55}Fe compounds after photoionization and K capture, respectively; (top) MnO (dotted), Mn_2O_3 (solid) and $KMnO_4$ (dashed); (middle) $^{55}Fe_2O_3$ (dotted), $K_3{}^{55}Fe(CN)_6$ (solid) and $K_4{}^{55}Fe(CN)_6$ (dashed); The instrumental broadening is larger for the ^{55}Fe K capture spectra than for the Mn systems after photoionization; (bottom) ligand field multiplet calculations for the ^{55}Fe compounds.

tions could be performed. We note, however, that symmetry mixing between wavefunctions with different spin states induced by spin–orbit interaction can yield intermediate spin states also for molecular wavefunctions. A theory that does not fully include such mechanisms might therefore give inaccurate results.

We also note that for correct calculation of the K fluorescence after photoionization it is necessary to include all populated 1s intermediate states as has been shown recently [30].

5.2. *Kα lines*

The spectral changes for Fe Kα lines are less pronounced than for Kβ emission (Fig. 9). The 2p and 3d orbitals interact less with each other than 3p and 3d because of the smaller overlap of the wave functions. To find a relation between the valence shell spin state and the spectral shape one could think of using the $K\alpha_1$ line energy position as it was done for the Kβ emission. However, multiplet theory suggests a different relation, namely that between the $K\alpha_1$ line width and the (2p,3d) exchange interaction. Assuming again a zero orbital angular momentum we find that the $K\alpha_1$ line is solely split by this exchange interaction and we

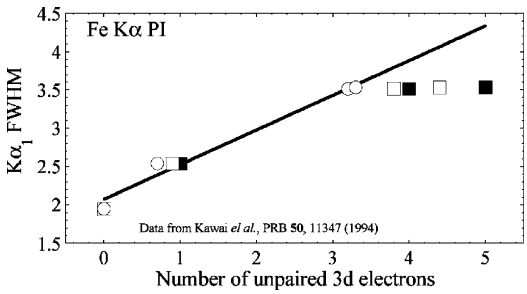

Fig. 10. Measured $K\alpha_1$ FWHM in Fe compounds after photoionization vs. number of unpaired 3d electrons [41]; (a) full boxes: nominal number of unpaired 3d electrons as derived from the Fe oxidation state, (b) empty boxes: the effective ground state number of unpaired 3d electrons, (c) circles: the effective 1s excited state number of unpaired 3d electrons. The linear regression is shown for (c) which gives the smallest standard deviation.

thus expect a linear relation between the $K\alpha_1$ full-width at half-maximum (FWHM) and the metal ion spin state [29].

Before analyzing the experimental $K\alpha_1$ FWHM we point to another problem that we have neglected so far. The matter becomes more complicated because the effective number of 3d electrons changes upon creation of a core hole. The electron cloud reacts to the change of the electron configuration on a time scale faster than the fluorescence decay occurs [89,88].[2] We thus obtain different numbers for $3d_{eff}$ depending on whether or not there is a core hole present in the metal ion electron configuration. The core hole effect is included in the ligand field multiplet approach by empirically introducing the core hole potential that acts on the 3d electrons [85]. In a very nice study, Kawai and coworkers investigated the effective spin in the ground state and in the 1s excited state of FeO, Fe_2O_3, $K_3Fe(CN)_6$ and $K_3Fe(CN)_6$ [41]. The effective number of 3d electrons was determined separately for both spin orientations by using a spin-unrestricted discrete-variational Hartree-Fock-Slater (Xα) molecular orbital method, which is a density–functional approach, and a subsequent population analysis. They found for FeO and Fe_2O_3 almost identical effective spin states in presence of a 1s core hole giving rise to very similar K fluorescence lines. If we compare plots of the $K\alpha_1$ FWHM versus the nominal and the two effective numbers of unpaired 3d electrons we find that only the latter as calculated for the complex in presence of a 1s hole, i.e. in the 1s excited state, yields the expected linear relationship (Fig. 10).

Kawai et al. pointed out that the effect of the core hole is less pronounced for covalent compounds because of the additional screening by the ligand electrons. Similar findings were published by Oku et al. who compared 2p XPS spectra to the Kα emission in Mn oxides and Fe cyanides [67]. Suzuki et al. published the calculated effective number of

[2] The term ‘electron relaxation’ is used in the literature to describe two different processes. It is either an electronic transition between two energy levels or the gradual adjustment of the electrons to a new potential, i.e. a new Hamiltonian with new energy levels. We refer here to the latter.

3d electrons for a large selection of transition metal oxides [50].

The core hole effect is a well-known problem and various theoretical approaches exist to include the core hole in the calculation of spectra from photoemission, absorption spectroscopy and K fluorescence main line emission [37,86,89–92].

5.3. Summary

We can draw some important conclusions from the analysis of the Kα and Kβ main lines that generally hold for inner-shell spectroscopy on transition metal complexes. First, the intra-atomic interactions as they are treated in multiplet theory are crucial for the understanding of the spectral shape. Second, electron–electron interactions between the core hole and the valence electrons have to be determined from the effective number of 3d electrons. Third, the effective number of 3d electrons should be calculated for the 1s excited state. This can be done in a configuration interaction approach including charge transfer or by referring to density–functional calculations with a subsequent population analysis. Both approaches have been applied to analyze the Fe L-edges of a series of non-heme Fe systems by Wasinger et al. [93].

The $K\beta_{1,3}$ peak position and the $K\alpha_1$ FWHM depend on the exchange interaction between the core hole and the unpaired spin in the valence shell. The examples that we have discussed exhibit an almost linear behavior and we find that the intra-atomic exchange splitting is the dominating interaction. We write the observed linear relationship in the following form:

$$\Delta E \propto S_{3d}^{\text{eff}} a \tag{2}$$

The exchange energy splitting ΔE is proportional to the effective spin in the atomic 3d orbitals S_{3d}^{eff} multiplied by the atomic or ionic exchange parameter *a* which is the averaged ((2,3)p,3d) exchange integral for a pair of (2,3)p and 3d electrons: [26,29]

$$a = \tfrac{2}{15} G^1_{(2,3)p3d} + \tfrac{3}{15} G^3_{(2,3)p3d} \tag{3}$$

In K fluorescence spectroscopy, the effective number of unpaired 3d electrons (effective spin) becomes the proportionality factor between the exchange parameter *a* and respectively the $K\beta_{1,3}$ first moment shift and the $K\alpha_1$ line width change. S_{3d}^{eff} incorporates the reduction factor of the Slater integrals if a multiplet picture is invoked. The exchange parameter *a* should be determined from the same atomic 3d orbitals that are used in the population analysis of the density–functional results. If the basis set is changed between different calculations and population analyses, one can normalize Δ*E* with respect to *a*.

We note that the assumed linear relation between the effective spin and respectively the $K\alpha_1$ FWHM and the $K\beta_{1,3}$ peak position neglects many-electron transitions, final state lifetime effects and influences of the metal site symmetry on the spectral shape (apart from those that affect the effective spin) [30,68,73]. A strictly linear behavior in the experimental spectra can therefore not be expected. Furthermore, the orbital angular momentum is not always fully quenched and the simple Eq. (2) is only approximately satisfied [34]. In most cases, the change of the $K\beta_{1,3}$ peak position and $K\alpha_1$ FWHM will still reflect a change of the effective electron spin on the metal ion. However, experimental results should always be critically analyzed with respect to the neglected mechanisms.

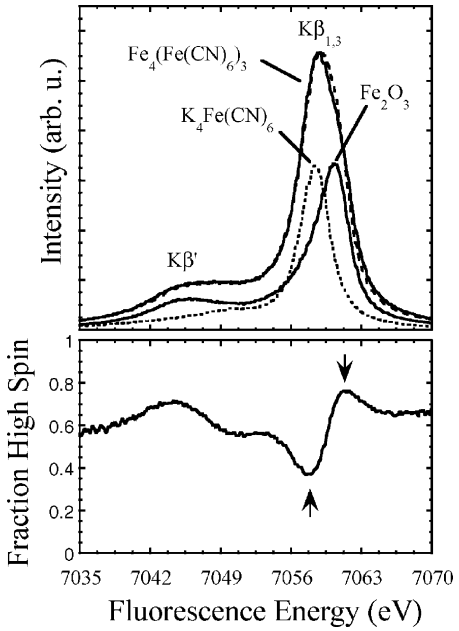

Fig. 11. (Upper panel, lower curves) Kβ spectra of Fe_2O_3 (solid line) and $K_4Fe(CN)_6$ (dotted line). The Fe_2O_3 and $K_4Fe(CN)_6$ spectra were normalized so that the ratio of the integrated intensities is 4:3, respectively, as is expected for the ratio high-spin Fe:low-spin Fe in PB. (Upper panel, upper curves) $Fe_4[Fe(CN)_6]_3$ spectrum (solid line) vs. normalized sum of Fe_2O_3 and $K_4Fe(CN)_6$ spectra (dashed line). (Lower panel) Estimated fraction of signal arising from high-spin Fe(III) component in the PB spectrum vs. fluorescence energy, using Fe_2O_3 and $K_4Fe(CN)_6$ as models. The arrows indicate the fluorescence energies where site-selective absorption spectra were taken. (reprinted with permission from ref. [60]).

6. Site-selective EXAFS

The chemical sensitivity of the $K\beta_{1,3}$ peak can be exploited to record site-selective EXAFS scans in mixed-valent compounds [60,94,95]. Here, the Kβ emission represents a superposition of the Kβ lines from the two different sites in the compound. As an example, we show in Fig. 11 the Kβ emission in Prussian Blue ($Fe_4[Fe(CN)_6]_3$). The spectra of Fe_2O_3 and $K_4Fe(CN)_6$ are also included as models for the Kβ lines from the high-spin and low-spin Fe sites in Prussian Blue. Their normalized sum is superimposed on the Prussian Blue spectrum. The site-selectivity is achieved by tuning the emission analyzer to a particular fluorescence energy. The fluorescence intensity is then recorded while the

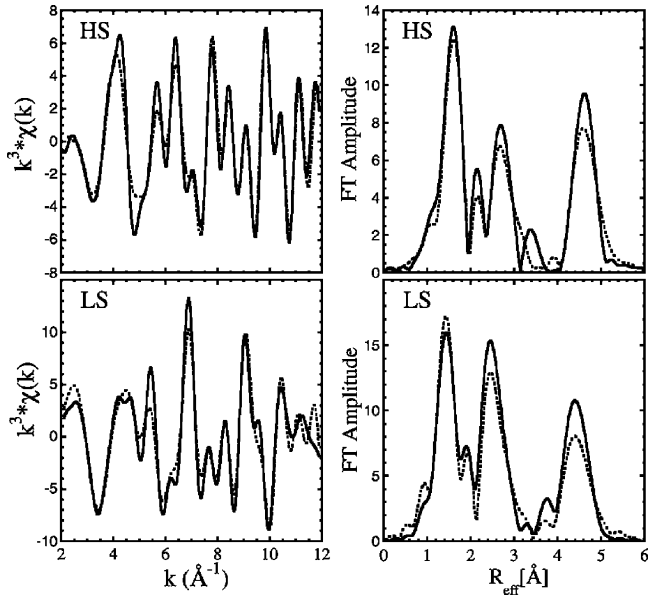

Fig. 12. Left: Deduced site-selective EXAFS spectra (solid lines) for the high-spin (top) and low-spin (bottom) site in PB with the corresponding EXAFS fits (dotted lines); right: Fourier transforms of the deduced EXAFS data with the corresponding fits. (reprinted with permission from ref. [60]).

incident energy is scanned across the Fe EXAFS range. The contributions from the different Fe sites in Prussian Blue to such a fluorescence-detected absorption scan depend on the chosen emission energy. The best site selectivity is achieved when the spectrometer is tuned to the fluorescence energies indicated by the arrows in Fig. 11.

The recorded EXAFS scans, however, do not represent the 'pure' spectra from the respective site because the Kβ lines from the two sites overlap. It is therefore necessary to apply a mathematical procedure based on singular value decomposition to extract the pure absorption scans that actually represent the two sites separately [60]. Fig. 12 shows the deduced Fe high-spin and low-spin EXAFS spectra in Prussian Blue. The fit reproduces the crystallographic distances with physical σ^2 values.

This technique to obtain site-selective EXAFS in mixed-valence compounds has the advantage of being potentially applicable to any type of sample that can be measured in conventional fluorescence detected absorption spectroscopy. The limitation arises from possibly insufficient separation of the fluorescence lines from the two sites. Possibly useful Kβ shifts generally exist between a metal and its oxidized forms—hence catalysis is one potential application area. High-spin low-spin systems are particularly suited for this technique because of the distinct change in effective spin and thus in the $K\beta_{1,3}$ spectrum.

Absorption spectroscopy using high-resolution fluorescence detection can also be used on other fluorescence features [96,97]. The $K\beta_{1,3}$ and Kβ′ peaks correspond to different spin orientations of the emitted photoelectron. Hence it is possible to record spin-selective K absorption edges [98–101]. The high photon flux on third generation storage rings enables to perform selective absorption studies even on the weak Kβ satellite structure. Here, the chemical shifts are more pronounced and some features are sensitive to the ligand species and/or exhibit an angular dependence (vide infra). This could be used to record ligand- and/or orientation-selective absorption scans in polycrystalline samples, respectively.

7. The Kβ satellite emission

Valence-to-core transitions (Kβ satellite lines) are obvious candidates for chemically sensitive fluorescence lines, since the character of the valence orbitals changes the most between different chemical species. In terms of atomic orbitals, spectral intensity is mainly expected from metal 4p as well as ligand np and ns ($n = 2, 3$) orbitals but it has been argued that also quadrupole 3d–1s transitions contribute [102]. It should be noted that ligand ns to metal 1s transitions are not dipole forbidden because the selection rules refer to orbitals with the same symmetry center, i.e. orbitals that belong to the same atom. We do not discuss many-electron transitions in detail as they have not yet been successfully used to study chemical dependence [24,103]. Furthermore, we neglect quadrupole contributions to the Kβ satellite spectral intensity since they are considerably weaker than dipole transitions. We do consider them in the K-edge absorption (vide infra) because the main edge (dipole) and pre-edge (mainly quadrupole depending on local symmetry) are sufficiently separated in energy making it possible to distinguish between the two types of transitions. To our knowledge, Kβ satellite emission lines in transition metal complexes due to quadrupole transitions have not yet been observed presumably due to the fact that dipole and quadrupole transitions are close in emission energies and cannot be resolved because of the core hole lifetime.

The Kβ satellite region is divided into the Kβ″ or 'cross-over' peak at lower fluorescence (or higher binding) energies and the $K\beta_{2,5}$ structure directly below the Fermi level. For Mn complexes, previous work on these spectral regions has been reported by Koster and Mendel [102], Mukoyama and Taniguchi [104], and Urch [105]. In the following we discuss the origins of the spectral features and the chemical information that can be obtained from the spectra.

7.1. The cross-over transition

7.1.1. Identifying ligands

The Kβ″ peak in transition metal complexes has long been assigned to ligand 2s to metal 1s cross-over transitions [105] and recently this has been systematically studied for Mn compounds with N, O and F ligands (Fig. 13) [106]. The relative shifts between the cross-over fluorescence energies for different ligands correspond mainly to the shifts in 2s binding energies of the atomic species. Therefore the cross-over peaks appear below the highest $K\beta_{2,5}$ feature (which indi-

cates the energy of the Fermi level) and are shifted by approximately the ligand 2s binding energies.

Furthermore, there is a strong dependence of cross-over intensity with metal ligand distance. This can be seen in the inset of Fig. 13, where the normalized Kβ″ intensities are plotted as a function of metal ligand distance for a series of Mn oxides. When normalizing the integrated Kβ″ intensity to that of the main Kβ region and to the number of ligands, an approximately exponential dependence can be observed over two orders of magnitude. Assuming that the integrated intensity per Mn of the main Kβ region is chemically invariant, this procedure yields the relative cross-over transition probability per Mn–O pair.

The strong sensitivity of Kβ″ to both ligand species and distance in particular for N, O, and F is a valuable complement to, e.g. EXAFS, where such a distinction is usually not possible. Furthermore one can think of using the Kβ″ spectral region for ligand-selective EXAFS studies similar to site-selective EXAFS discussed in Section 6.

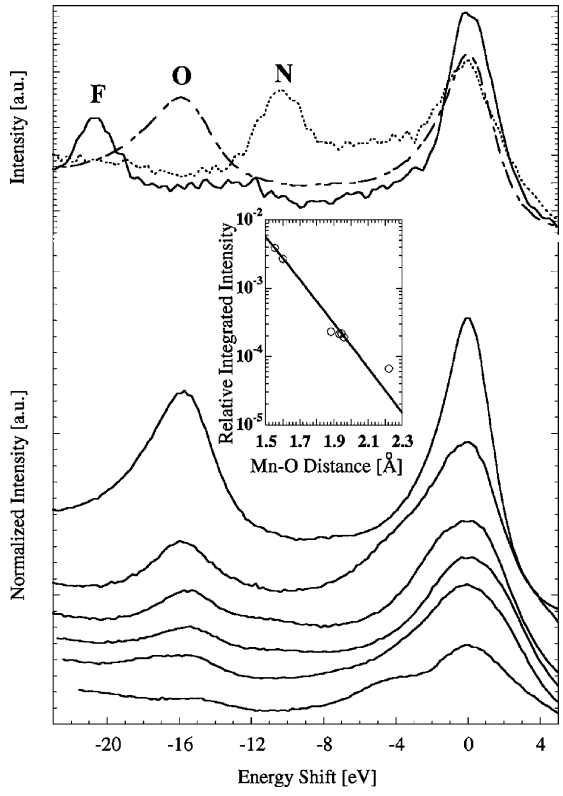

Fig. 13. (top) Kβ″ and $K\beta_{2,5}$ regions for samples with Mn–F, Mn–O, and Mn–N ligation. The energy zero has been shifted to put the main peak of the $K\beta_{2,5}$ line at 0 eV; (bottom) Kβ″ and $K\beta_{2,5}$ regions of manganese oxides with different Mn oxidation states. The spectra have been shifted to coincide at the Fermi level. Top to bottom: $KMn^{VII}O_4$, $[Et_4N][Mn^{V}(O)(\eta 4\text{-}L)]$, β-$Mn^{IV}O_2$, $LiMn^{III}Mn^{IV}O_4$ and $ZnMn^{III}{}_2O_4$, $Mn^{II}O$, $Li_2Mn^{IV}O_3$. The intensities are normalized to the Kβ main line intensity in the region from 6463 to 6505 eV fluorescence energy; (inset) Normalized intensities of Kβ″ as a function of Mn–O distance. The integrated normalized intensities as shown for some compounds at the bottom are further divided by the number of O-ligands per Mn to represent the interatomic transition probability per Mn–O pair. The solid line is the least squares fit using an exponential type distance dependence. (reprinted with permission from reference [106]).

7.1.2. Angular dependence

The non-resonant dipole K fluorescence emission from polycrystalline samples is isotropic. A single crystal, however, exhibits an angular and polarization dependent emission that can be exploited to obtain information about the spatial orientation of the valence molecular orbitals. Dräger and co-workers analyzed the polarization of the fluorescence emission in single crystalline complexes [107–109]. We review here the angular dependence of Kβ satellite spectra. Before discussing the experimental results, we give a brief account of the theoretical treatment using Fermi's Golden Rule in the dipole approximation.

In the sudden approximation one can factorize the *N*-electron wave functions that describe the initial and final state, respectively, as $\Psi_i^N = \varphi_i \psi_i^{N-1}$ and $\Psi_f^N = \varphi_f \psi_f^{N-1}$ [110]. The one-electron wave functions φ describe the orbitals that are directly involved in the transition, i.e. the transition operator only acts on these orbitals. For the Kβ satellites, the fluorescence initial state is the 1s excited state $1s3d^n$ and φ_i identifies with a 3d or, more generally, a valence orbital (VO). Likewise, φ_f identifies with the 1s wave function. Barth and Grossmann pointed out that the energies and wave functions have to be determined for the fully relaxed states, i.e. the influence of the core hole has to be considered ('Final State Rule') [111].

In a one-electron, sudden approximation picture one can therefore estimate the intensities for a Kβ satellite spectrum by writing [12,14]

$$dW_{if} \propto \omega_{if}^3 \sum_{\lambda} |\langle \varphi_f^{1s} | \hat{\varepsilon}_\lambda \vec{r} | \varphi_i^{VO} \rangle|^2 d\Omega \tag{4}$$

where φ_i^{VO} describes a valence electron orbital as obtained in the 1s excited (Kβ initial) state, φ_f^{1s} describes a 1s electron orbital as obtained in the Kβ final state with a filled 1s shell and hole in a valence orbital, $\hat{\varepsilon}_\lambda$ is the polarization vector of the outgoing photon with the sum extending over the polarization directions, $\vec{r}$ is the position vector of an electron referred to the nucleus and ω_{if} is the frequency for the energy difference E_i–E_f between the initial and final state. For simplicity we assume that we employ a point-like emission analyzer (in practice the solid angle is $\pm 1.5^\circ$ for one analyzer crystal). Furthermore, the experiments are performed for the extreme cases, i.e. near the minima or maxima of the $\sin^2$ or $\cos^2$ functions where dW_{if} only shows small variations. We therefore do not perform the integration over the solid angle. The differential transition rate dW_{if} can be used to obtain the Kβ satellite spectrum of a single crystal.

As an example we discuss the angular dependence of the Kβ satellite emission in an oriented single crystalline Mn nitrido complex $[Rh(en)_3][Mn(N)(CN)_5]\cdot H_2O$ [73]. As shown in Fig. 14, the Mn atom is surrounded by five cyanide groups and one nitrogen (nitrido). The structure of the complex is

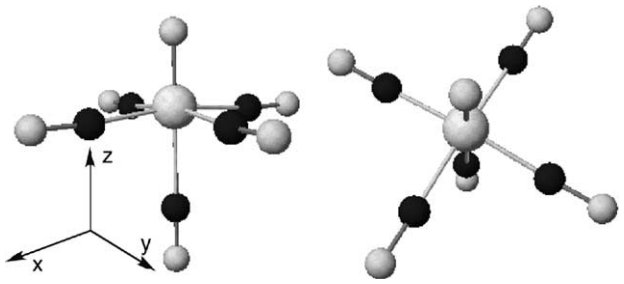

Fig. 14. Structure of Mn nitrido complex $[Mn(N)(CN)5]^{3-}$. The Mn-nitrido bond is oriented along the *z*-direction. The four cis cyanide groups and the Mn atom do not lie in a plane (the *xy*-plane) but the four cyanide groups are displaced by 0.19 Å away from the nitrido in negative *z*-direction.

best approximated by the point group C_{4v} and the molecular structure suggests a strong spatial orientation of the molecular orbitals. The short Mn–N bond length at 1.50 Å in *z*-direction results in a large overlap between the Mn 1s and the nitrido orbitals and the nitrido contribution to the Kβ satellite emission is expected to be large.

We define θ as the angle between the crystal *z*-axis and the propagation vector $\vec{k}$ of the emitted X-rays. The propagation vector is perpendicular to the plane spanned by the two possible polarization directions of $\hat{\varepsilon}_\lambda$ in Eq. (4). The Kβ satellite lines after 1s photoionization of the oriented single crystal were measured for two different orientations of the Mn-nitrido axis relative to the analyzer crystals (Fig. 15). The peak at 0 eV relative fluorescence energy for $\theta = 90^\circ$ is the Kβ″ or 'cross-over' peak. Following the arguments in the previous section, we assign it here to a nitrogen 2s to metal 1s transition. Its exact molecular orbital origin will be analyzed below using density–functional theory. The structures at higher energies are the $K\beta_{2,5}$ lines. The cross-over peak disappears at $\theta \sim 8^\circ$. The $K\beta_{2,5}$ feature shows two 'bands' separated by about 2.7 eV. A similar $K\beta_{2,5}$ structure has been observed for Fe cyanides (vide infra). The relative intensities of the two bands vary between the two angles: the band at higher energies gains in intensity relative to the band at lower energies for $\theta \sim 90^\circ$.

One can now analyze the transition matrix elements for the two extreme cases $\theta = 0^\circ$ and $\theta = 90^\circ$. We use the notation $\langle\varphi_f^{1s}|(x, y, z)|\varphi_i^{VO}\rangle = |(x, y, z)_{if}|$ for the transition matrix elements that are obtained from the $\hat{\varepsilon}\vec{r}$ operator in Eq. (4) using the polarization direction unit vectors $\hat{x}$, $\hat{y}$ and $\hat{z}$. In our case we obtain $|x_{if}|^2 = |y_{if}|^2$ because of the rotational symmetry C_{4v} around the *z*-axis. The two polarization directions for $\theta = 0^\circ$ (i.e. the wave vector $\vec{k}$ pointing along the *z*-direction) are $\hat{x}$ and $\hat{y}$. The two polarization directions for $\theta = 90^\circ$ (i.e. the wave vector $\vec{k}$ pointing along the *x*- or *y*-direction) are $\hat{x}$ or $\hat{y}$ and $\hat{z}$. One thus obtains for the transition rate for the two extreme cases:

$$\theta = 90^\circ: \quad dW_{if} \propto \omega_{if}^3(|x_{if}|^2 + |z_{if}|^2) \tag{5}$$

and

$$\theta = 0^\circ: \quad dW_{if} \propto \omega_{if}^3 2|x_{if}|^2 \tag{6}$$

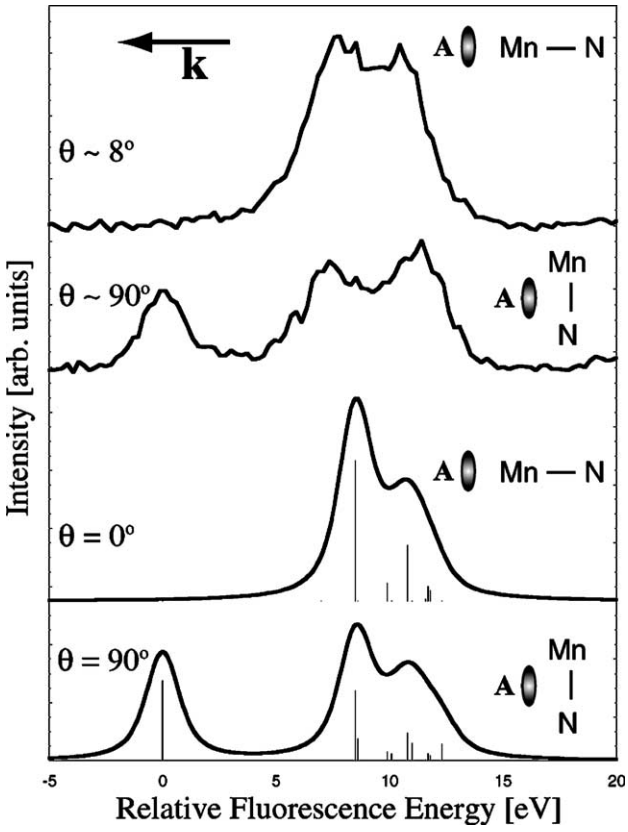

Fig. 15. Mn Kβ satellite lines in $[Rh(en)_3][Mn(N)(CN)_5]\cdot H_2O$. The top two spectra show the experimental results after 1s photoionization. The tail of the $K\beta_{1,3}$ peak was subtracted and the spectra are normalized to each other in the entire Kβ spectral area. The bottom two spectra show the corresponding calculations for the two angles. A 1.2 eV Lorentzian and 1.3 eV Gaussian broadening were applied to the stick spectra to account for the lifetime and instrumental broadening, respectively. The experimental and theoretical spectra are aligned in the cross-over peak. For each spectrum, the respective orientation between the Mn-nitrido axis and the analyser (*A*) is given and the direction of the propagation vector $\vec{k}$ is shown.

A qualitative analysis of the transition probabilities can now be attempted using symmetry arguments. The point group that describes the local symmetry around the Mn atom is C_{4v}. There are five irreducible representations (irreps) in C_{4v} namely A_1, A_2, B_1, B_2 and E. Any eigenstate (i.e. wavefunction of specific energy) of the Hamiltonian describing the system must transform according to an irrep of the point group, i.e. each molecular orbital has to transform under the symmetry operations in C_{4v} like one of the five irreps. The coordinates (*x*, *y*, *z*) can also be assigned to these irreps and one finds that (*x*, *y*) transform as E and *z* transforms as A_1. In order for a transition to be orbitally allowed the direct product $\Gamma_f\Gamma_{xyz}\Gamma_i$ (where Γ represents an irrep) that arises from the transition matrix element $\langle\varphi_f^{1s}|(x, y, z)|\varphi_i^{VO}\rangle$ has to contain the identity (totally symmetric) representation A_1. The Mn 1s orbital branches to A_1 in C_{4v}. Determining the direct product one finds that only the symmetries $\Gamma_f = A_1$ and E of the valence electron orbitals yield non-zero transition integrals, i.e. only the combinations $A_1A_1A_1$ and A_1EE

give rise to spectral intensity. For $|z_{if}|^2$ we obtain A_1 and for $|x_{if}|^2$ E symmetry for the valence electron orbital with non-zero transition integrals.

We now compare this analysis to the experimental results. The cross-over peak disappears when the Mn-nitrido axis points towards the analyzer crystals, i.e. $\theta = 0°$, and we only have contributions from $|x_{if}|^2$ (A_1EE) as expressed in Eq. (6). This in turn means that the spectra do not show any transitions resulting from valence orbitals with A_1 symmetry. The spectrum taken at $\theta \sim 8°$ shows mostly transitions from valence orbitals with E symmetry (except for a small A_1 contribution since θ is not exactly zero). It can thus be concluded that the valence orbital that can be assigned to the cross-over peak has A_1 symmetry. On the other hand, the spectrum taken at $\theta \sim 90°$ shows equal contributions from E and A_1 symmetry.

One can be more quantitative by calculating the transition matrix elements from the molecular orbital that can be determined using density–functional theory [45]. One can approximate the molecular wavefunctions as linear combinations of atomic orbitals by means of a population analysis. It is thus possible to assign the transition intensity to atomic orbitals that either belong to the metal ion or the ligand. The calculated spectra are shown in Fig. 15 [73]. The angular dependence of the cross-over peak, the two bands in the $K\beta_{2,5}$ structure as well as the relative energy splittings are well reproduced. The molecular orbital that gives rise to the cross-over peak has A_1 symmetry in the calculations and is formed to 86% by the nitrido 2s orbital. The calculations show that the magnitude of ligand orbital to metal 1s transition matrix elements can reach up to 20% of Mn 4p–1s transitions. Since the Mn 4p contribution to the composition of the molecular orbitals is less than 15% we find that both, the Mn 4p and ligand orbitals, are equally important in the Kβ satellite spectra.

The relative intensities between the two $K\beta_{2,5}$ bands are poorly simulated in the calculations. We can explain the disagreement between theory and experiment with the numerous approximations in the theoretical model such as small cluster size and neglect of electron–electron interactions as well as multi-electron excitations. Particularly consideration of the latter is a formidable task in theoretical models that calculate the electron density. We can use, however, the K capture decay to reduce the influence of multi-electron transitions as we will show in the next section.

7.2. Valence electron perturbation upon 1s photoionization

When discussing the Kα and Kβ main lines we pointed out the importance of the core hole effect and its influence on the effective number of 3d electrons. We neglected however thus far the valence electron perturbation that is caused during photoionization of the metal 1s shell. Any electronic transition in an atom causes a readjustment of the passive electrons, i.e. those that are not directly involved in the transition, to the perturbed potential. A passive electron in an orbital φ_μ^i before the perturbation will relax into an orbital $\varphi_{\mu'}^f$. In a so-called adiabatic relaxation we have $\mu = \mu'$, i.e. initial and final state orbitals are described by the same set of quantum numbers. If the relaxation is non-adiabatic, the electron will occupy an orbital with different quantum numbers ($\mu \neq \mu'$). Those transitions can be referred to as shake or multiple electronic transitions [32,112,113]. The 1s electrons screen the nuclear charge and the valence electrons only experience a reduced effective nuclear charge. A removal of one of the 1s electrons causes a considerable change of the effective potential. The orbitals will adjust and with some probability shake transitions will occur (Fig. 16).

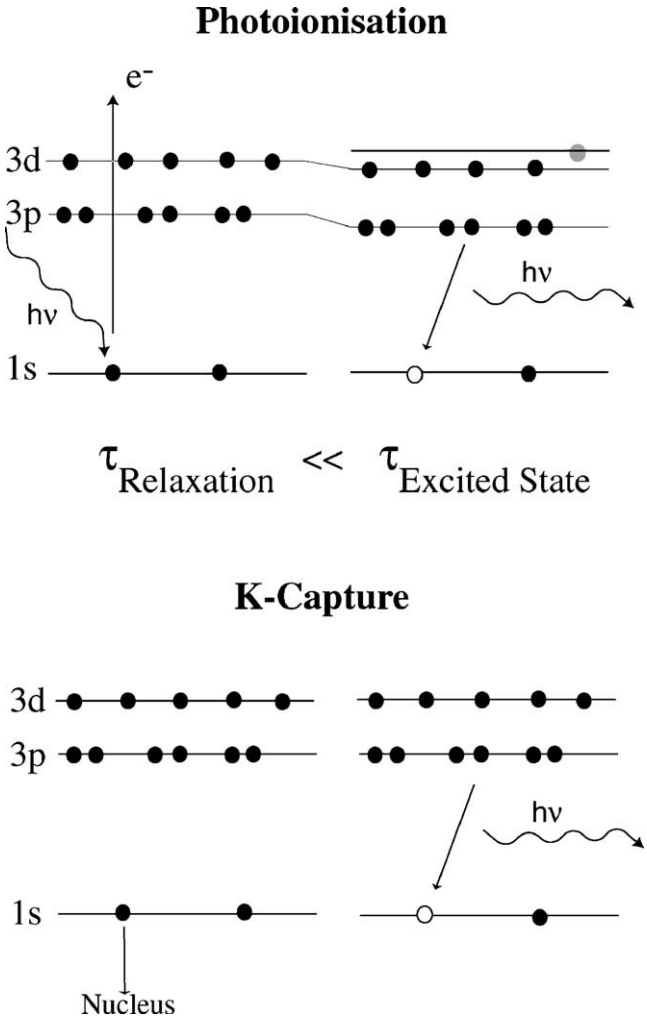

Fig. 16. Simplified illustration of the relaxation process after photoionization (top) and after K capture decay (bottom). The 3d and 3p orbitals adjust to the new effective nuclear potential after photoionization. A non-adiabatic relaxation in the valence orbitals is shown with one electron occupying a higher orbital. No relaxation occurs after K capture because the 1s hole is compensated by the decrease in nuclear charge in terms of the effective potential experienced by the 3p and 3d electrons.

Shake transitions are an interesting phenomena for the physicist who is interested in fundamental processes, but they can represent a serious problem for the physical chemist

who wants to study the ground state properties. We can investigate shake transitions experimentally by comparing the two modes of 1s core hole creation. The 1s electron in K capture decay annihilates with a proton in the nucleus. Thus a negative and positive charge disappear unlike in 1s photoionization where only a 1s electron is removed from the atom. The effective potential that is experienced by the 3d electrons thus hardly changes during a K capture decay. Without orbital relaxation no shake transitions will occur in the 1s core hole creation process (Fig. 16). Eventually relaxation will occur also after K capture decay. The decay results in a Mn impurity in a Fe-ligand lattice. Consequently, the system will relax to adjust to the new situation. However, the lattice relaxation time of the nuclei is expected to be much slower than the lifetime of an excited electronic state. Furthermore, the relaxation will start only after the core hole is filled, i.e. when the effective nuclear charge does not resemble an Fe nucleus anymore. We can therefore neglect relaxation processes after K capture decay of ^{55}Fe in inner-shell spectroscopy. We note that care has to be taken when other K capture isotopes are used with a larger Q value and considerable recoil energy that can result in a large distortion of the structure within the core hole lifetime.

A study of the Kβ main lines in MnO after photoionization and in $^{55}Fe_2O_3$ after K capture reveals spectral differences between the two modes of 1s core hole creation [30,114]. Taking shake transitions in the photoionization process into account it was possible to simulate the spectra based on a ligand field multiplet approach including configuration interaction. We expect shake transitions to have an even stronger effect on the spectral shape in the Kβ satellite emission where the valence orbitals are probed directly. The Kβ satellite spectra in a series of Fe compounds after photoionization and after K capture decay are shown in Fig. 17.[3] The overall spectral shape of Kβ″ and $K\beta_{2,5}$ features are similar in both excitation modes but the peaks in the K capture spectrum appear considerably sharper than in the photoionization spectrum and the intensity ratios of the two $K\beta_{2,5}$ bands in the cyanides differ.

The orbital relaxation after photoionization can cause shake transitions that give rise to redistribution of spectral intensity and population of valence orbitals that remain unoccupied in the K capture technique. We cannot distinguish the different orbitals in the Kβ satellite spectra because the lines merge into each other due to the core hole lifetime. The additional orbitals that are occupied in the shake process during photoionization thus mainly result in a broadening of the spectral features. The shake transitions

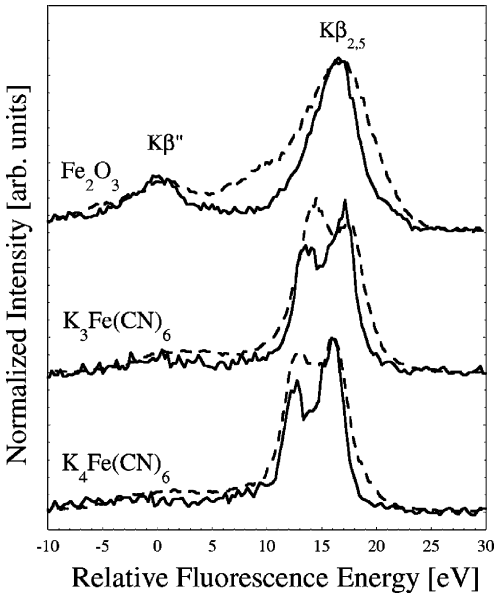

Fig. 17. Kβ satellite lines in a series of Fe compounds measured after K capture (solid lines) and photoionization (dashed lines). The energy scales are different in the two techniques and were aligned in the F_2O_3 Kβ″ peak.

can also partly explain the differences between theory and experiment in the Mn nitrido complex that we discussed in the previous section.

We can validate our arguments by using a comparison to valence band photoemission spectra (XPS) in Fig. 18. The Kβ satellite transitions and valence photoemission result in the same final state configurations with one valence electron removed from the ground state configuration. While Kβ emission reaches this state in a two-step process they are directly reached in XPS without the need of a core hole creation. The assignment of the XPS spectral features was confirmed by several authors using ligand field and density–functional calculations [116,117]. Similar to the Mn-nitrido complex (Section 7.1.2) we expect intensity from the O 2s and 2p orbitals to contribute to the Kβ satellite spectra. However, the Fe 3d states can only be observed in the photoemission but not in the Kβ spectrum because of the dipole selection rules.

We thus find that the results from K capture Kβ satellite emission are consistent with the valence electron configuration as obtained from valence band photoemission. The 1s core hole effect can therefore be neglected in K capture spectroscopy. Shake transitions have to be accounted for in the 1s photoionization process. The core-hole potential shifts the Fe and ligand orbitals relative to each other in energy [30]. As a result, the energy levels as well as orbital hybridization change giving rise to new emission lines. From this point of view K capture decay is the preferable technique to study the electronic structure in K emission spectroscopy. However, experimentally it has some limitations. The technique involves radiochemistry and the data acquisition time can take up to a week for the spectrum of a 1 mCi

[3] For the Kβ main fluorescence lines, we compare Mn photoionization to Fe K capture because the magnitudes of the electron–electron interactions that shape the spectra strongly depend on the nuclear charge (^{55}Fe decays into a Mn nucleus). The Kβ satellite lines reflect molecular orbitals and band formation, respectively. In this case, we therefore compare identical compounds, i.e. Fe after K capture with Fe after photoionization because the spectral shape mostly depends on the local symmetry.

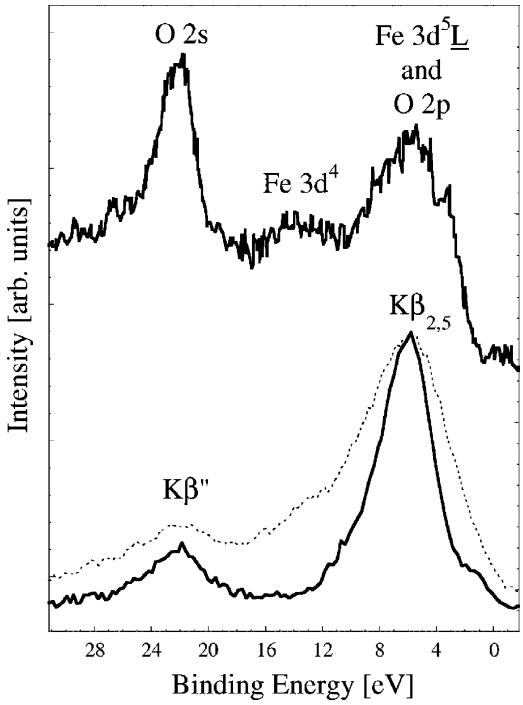

Fig. 18. Comparison of valence-band XPS (top) with Kβ satellite emission after K capture (bottom solid) and photoionization (bottom dotted). The spectra are aligned relative to each other in the oxygen 2s peak and the binding energy scale is taken from the XPS spectrum. The XPS data were taken by Fujimori et al. [115].

sample. On the other hand, photoionization spectra taken at a storage ring can be obtained in minutes to hours and have no restriction in terms of sample preparation and handling. But their detailed interpretation requires a thorough theoretical treatment of the relaxation process. Multi-electron excitations are a well-known problem and various theoretical approaches exist to include non-adiabatic relaxations in the calculation [32,37,86,100].

8. Resonant inelastic X-ray scattering (RIXS)

The electronic states that give rise to the edge of an absorption spectrum are resonantly excited states that subsequently decay. The energy that is released in the decay process can be carried either by an electron that is promoted into the continuum (resonant Auger effect) or by a photon (resonant X-ray scattering or RXS). The combination of resonant excitation with emission detection bears some interesting physical phenomena, such as interference effects, line narrowing and Raman–Stokes line shifts. An review of the resonant Auger effect was published by Armen [118]. A large body of work also exists on resonant X-ray scattering that was reviewed comprehensively by Kotani and Shin and Gel'mukhanov and Ågren [18,119]. We will focus in this article on applications at the transition metal K pre-edges where only few studies have been carried out until now. In the following sections we will refer to previous work known to us, however, the field has become very active recently and our references might be incomplete.

The local electronic configuration of the metal ion is reflected in the pre-edge region which arises from resonant excitations into the lowest unoccupied electronic states. The K pre-edge spectral features are sensitive to the metal oxidation state, the site symmetry and the crystal field splittings. Unfortunately, the intensity is usually very small compared to that of the main edge. A separation and subsequent analysis of the K pre-edge in conventional absorption spectroscopy is thus connected with a rather large uncertainty, in particular for early transition metals because the splitting between the pre-edge and main edge decreases with decreasing atomic number *Z*.

In the following we outline the concept of resonant inelastic X-ray scattering at the K absorption pre-edge in non- or polycrystalline transition metal complexes. Since most readers will not be familiar with RIXS we discuss the RIXS plane and its various aspects in general terms before we present experimental results. We show how RIXS spectroscopy facilitates separation of the pre-edge from the K main edge and give examples where previously unknown spectral features could be resolved. The spectral shape along the *energy transfer* of the scattered X-rays contains information on the metal spin state and thus complements the chemical information in the K pre-edge absorption features along the *incident energy*. A ligand field approach including multiplet interactions can account for the RIXS spectral features at the K pre-edge.

8.1. The RIXS process

In 1s(2,3)p RIXS, the incident energy is tuned to a 1s resonance and the subsequent radiative 2p or 3p–1s decay is recorded using a crystal analyzer of the type as discussed in Section 4. Ideally, the energy bandwidth of the analyzer is similar to that of the primary monochromator at the storage ring beamline and smaller than the lifetime broadening of the spectral features. The process can be viewed as an inelastic scattering of the incident photon at a resonance energy of the metal ion and is theoretically described by the Kramers–Heisenberg formula [18,119]

$$F(\Omega,\omega) = \sum_{\mathrm{f}} \left| \sum_{n} \frac{\langle f|T_2|n\rangle\langle n|T_1|g\rangle}{E_g - E_n + \Omega - i\,\Gamma_K/2} \right|^2 \times \frac{\Gamma_{\mathrm{f}}/2\pi}{(E_g - E_f + \Omega - \omega)^2 + \Gamma_{\mathrm{f}}^2/4} \tag{7}$$

This description is analogous to optical resonance Raman spectroscopy [120,121]. The instrumental energy bandwidth in RIXS as discussed in this review is of order 1 eV as compared to a few meV in optical Raman spectroscopy. The aim of resonant inelastic X-ray scattering or X-ray resonance Raman spectroscopy (XRRS) therefore is to study electronic

states rather than vibrational levels. Higher resolution in RIXS is possible, however, at the expense of lower photon counts.

The intermediate state $|n\rangle$ in Eq. (7) is reached from the ground state $|g\rangle$ via a transition operator T_1. In a simplified picture using atomic configuration we can write $|g\rangle = 3d^n$ and $|n\rangle = 1s3d^{n+1}$, i.e. a 1s electron is resonantly excited into a 3d orbital. The intermediate states $|n\rangle$ in RIXS spectroscopy are the final states in conventional K-edge absorption spectroscopy.

The form of the transition operator T_1 depends on the local symmetry of the metal ion in the ligand environment. The spherical (SO_3) symmetry of the atomic 3d orbitals branches to the lower symmetry at the metal site. If the symmetry is such that 3d and 4p orbitals do not mix then T_1 identifies with the quadrupole transition operator $(\hat{\varepsilon}_\lambda \vec{r})(\vec{kr})$ because the dipole transition matrix elements between the metal 1s and lowest valence orbitals are zero. This is, for example, the case when the scattering atom is six-coordinated with identical ligands in an octahedral geometry (O_h symmetry) where the metal 3d orbitals split into t_{2g} and e_g orbitals. In general, 3d (*gerade*) and 4p (*ungerade*) orbitals do not mix in complexes with inversion symmetry at the metal site and dipole transitions from the 1s to the lowest valence orbitals are so-called Laporte forbidden. Even if inversion symmetry is absent, a dipole transition might still be orbitally forbidden (for selection rules using the direct product of group theory see Section 7.1.2) [122].

The K pre-edge can obtain intensity from dipole transitions under certain conditions. If the symmetry is reduced, e.g. to C_{4v} by replacing one of the ligands with a different element or to tetrahedral (T_d) symmetry with four ligands, T_1 also includes the dipole operator $\hat{\varepsilon}_\lambda \vec{r}$. In this case, the crystal field split 3d orbitals partly belong to the same irreducible representation of the point group as the metal 4p orbitals [34,122,123]. The states can therefore mix and transitions from 1s to 3d4p mixed states are dipole allowed. The K pre-edge intensity thus indicates the local symmetry at the metal site. This was used by e.g. Wilke et al. and Westre et al. to characterize Fe minerals and coordination complexes [124,125].

The ratio of dipole to quadrupole contribution can be determined by means of several different techniques. The most common method is to analyze the angular dependence of the absorption coefficient in single crystalline samples using linear polarized light [126–132]. Resonant enhancement in the X-ray diffraction at a forbidden reflection (anomalous X-ray scattering) can also give evidence of quadrupole transitions [133–135]. The technique was used by Finkelstein et al. [136] in α-Fe_2O_3 and by Murakami et al. [137] in $LaMnO_3$ to determine the dipole contribution to the K pre-edge [138]. Resonant Auger spectroscopy was suggested to be capable of unraveling dipole and quadrupole contributions even in powdered samples [139]. A ligand field multiplet analysis of the Fe K absorption pre-edge by Westre et al. convincingly demonstrates the importance of both, dipole and quadrupole transition matrix elements, depending on the local symmetry at the metal site [125]. In an elaborate theoretical analysis of the Fe pre-edges, Arrio et al. included p–d hybridization in the ligand field multiplet model and determined the dipole contribution to the pre-edge spectral intensity [140].

RIXS spectroscopy can be used to separate the pre-edge structure from the K absorption main edge as we will show below. This allows for a more detailed look at the pre-edge spectral shape than in conventional absorption spectra and thus a better comparison with theoretical models. Furthermore, 1s2p RIXS in transition metals exhibits an angular dependence that is different for dipole and quadrupole transitions [141,142]. However, to our knowledge no attempt to determine the dipole-quadrupole ratio has yet been made using RIXS at the K pre-edge and remains as a task for the future. In this review we neglect the angular dependence of the scattering cross section.

The final states in Eq. (7) are reached via a 2p or 3p–1s transition and T_2 therefore identifies with the dipole operator. The RIXS final state configurations $|f\rangle$ are $(2,3)p^5 3d^{n+1}$ with a core hole in the 2p or 3p shell and an additional electron in a 3d orbital. They are formally identical to the soft X-ray L- and M-edge absorption final states, respectively. Thus, the question arises whether RIXS enables to record 'L-edge' and 'M-edge' like spectra combined with the advantages of bulk sensitive hard X-rays. The final states in RIXS spectroscopy with a core hole are reached via two transition matrix elements compared to a one step 2p or 3p–3d transition in the L- or M-edge absorption process. Other $(2,3)p^5 3d^{n+1}$ final states can be reached in RIXS due to different selection rules and the line intensities will differ because of different transition matrix elements and interference effects (vide infra) [143]. Even with equal instrumental resolution in both experiments, one can therefore not expect to obtain identical spectra using the two techniques. However, the energy splittings due to crystal field, multiplet and spin–orbit interactions are equal in both techniques. This implies that similar information can be gained from the two spectroscopies.

The RIXS process as depicted in Fig. 19 appears to be a two-step process separated into a resonant excitation to an intermediate state and a subsequent decay into a final state. We can explain the line-narrowing effect and the Raman–Stokes line shift in this simple two-step picture as we will show below. A close look at the Kramers–Heisenberg equation, however, tells us that this picture is not entirely correct [144,145]. The spectral intensity in an absorption or emission spectrum is proportional to the square of the transition matrix element [12]. However, for the RIXS process we have to add the products of the absorption and emission transition matrix elements before the square is formed for all scattering paths with the same final but different intermediate states (cf. Eq. (7), we neglect the polarization dependence). Absorption and emission are thus connected coherently and different intermediate states can interfere with each other. This interference can lead to a decrease in spectral intensity

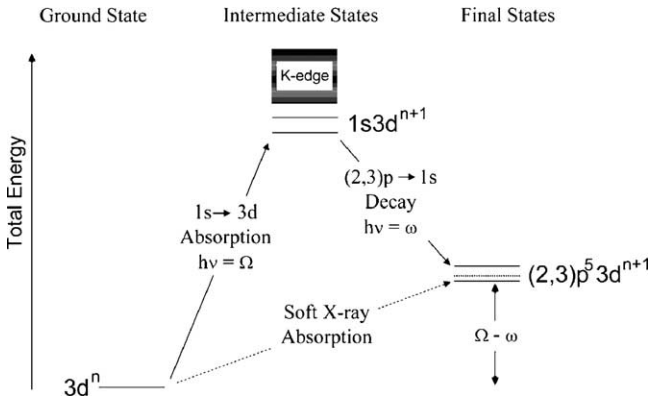

Fig. 19. RIXS energy scheme for 1s(2,3)p RIXS in a transition metal ion. The vertical axis describes the total energy of the electron configuration. For simplicity, atomic configurations are used and only 1s–3d excitations are shown.

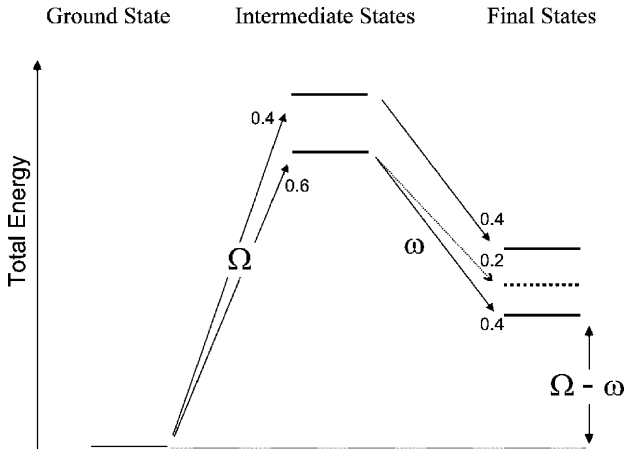

Fig. 20. Energy scheme for a model system. The relative transition intensities are given. The corresponding RIXS plane is shown in Figs. 21 and 22.

if absorption and emission matrix elements carry opposite signs. Numerous studies have been carried out to investigate interference effects in molecules due to nuclear dynamics [146]. The theory of RIXS in broad band solids which gives momentum conservation assumes interference between all equivalent lattice positions within the coherent X-ray field [147,148]. However, this does usually not apply to coordination complexes where band structure effects are negligible. Interference effects using a cluster model as theoretical approach were suggested by de Groot in CaF_2 [149]. To our knowledge, interference effects have not yet been systematically investigated in RIXS at the K pre-edge of transition metals.

8.2. The RIXS plane

The incident energy Ω as well as the emitted energy ω are varied in a RIXS experiment. The recorded intensity is proportional to $F(\Omega, \omega)$ (cf. Eq. (7)) and is thus plotted versus a two-dimensional grid. In order to assign the total energy of an electronic state to the axes of the contour plots we will use the energy transfer or final state energy Ω–ω as opposed to the emitted energy ω (cf. Fig. 19). The energy transfer axis relates to the excitation energy in L- and M-edge absorption spectroscopy, respectively. Eq. (7) contains two Lorentzian line shapes for the incident energy Ω and the energy transfer Ω–ω. The lifetime broadenings (full width at half maximum (FWHM)) Γ_K for the intermediate states and Γ_f (f = L, M) for the final states thus apply in the Ω and Ω–ω direction, respectively. An experimental spectrum will be further broadened by the energy bandwidths of the incident energy monochromator and the crystal analyzer.

We illustrate some aspects of RIXS spectroscopy in the following by discussing a theoretical RIXS plane for a model system. The RIXS spectrum can be shown as a surface plot (Fig. 21) or a contour plot (Fig. 22 bottom left). Since we will focus in the analysis of the experimental spectra on energy shifts and line splittings it is more instructive to use the contour plots. We use $\Gamma_K = 1.1$ eV and $\Gamma_L = 0.5$ eV for the Mn lifetime broadenings [150]. The example shows how the lifetime broadenings shape the peaks in the RIXS plane. Their spectral profiles are symmetric in the incident energy and energy transfer direction.

The physical meaning of the horizontal and vertical direction in the RIXS plane can be understood in connection with the energy scheme in Fig. 20. The total energy of the intermediate state electron configuration increases in the incident energy direction. A larger energy transfer corresponds to a larger final state energy. A resonance at a higher incident energy Ω will decay into a final state with a higher final state energy Ω–ω if the excited electron remains in the same valence orbital during the (2,3)p–1s decay, i.e. it observes the transition as a spectator electron (Fig. 21). The resonant 1s excitations thus appear on a diagonal line in the (Ω, Ω–ω) RIXS plane at constant emission energy ω.

The theoretical model system in Fig. 22 shows two resonances on the diagonal line at 6542 and 6544 eV incident

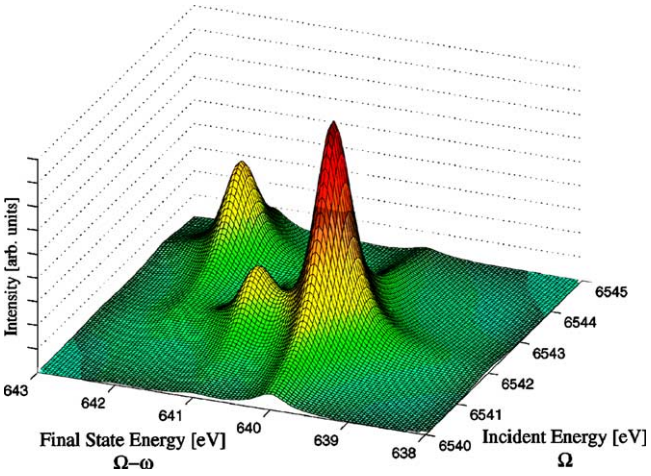

Fig. 21. Surface plot of the RIXS plane based on the energy scheme in Fig. 20.

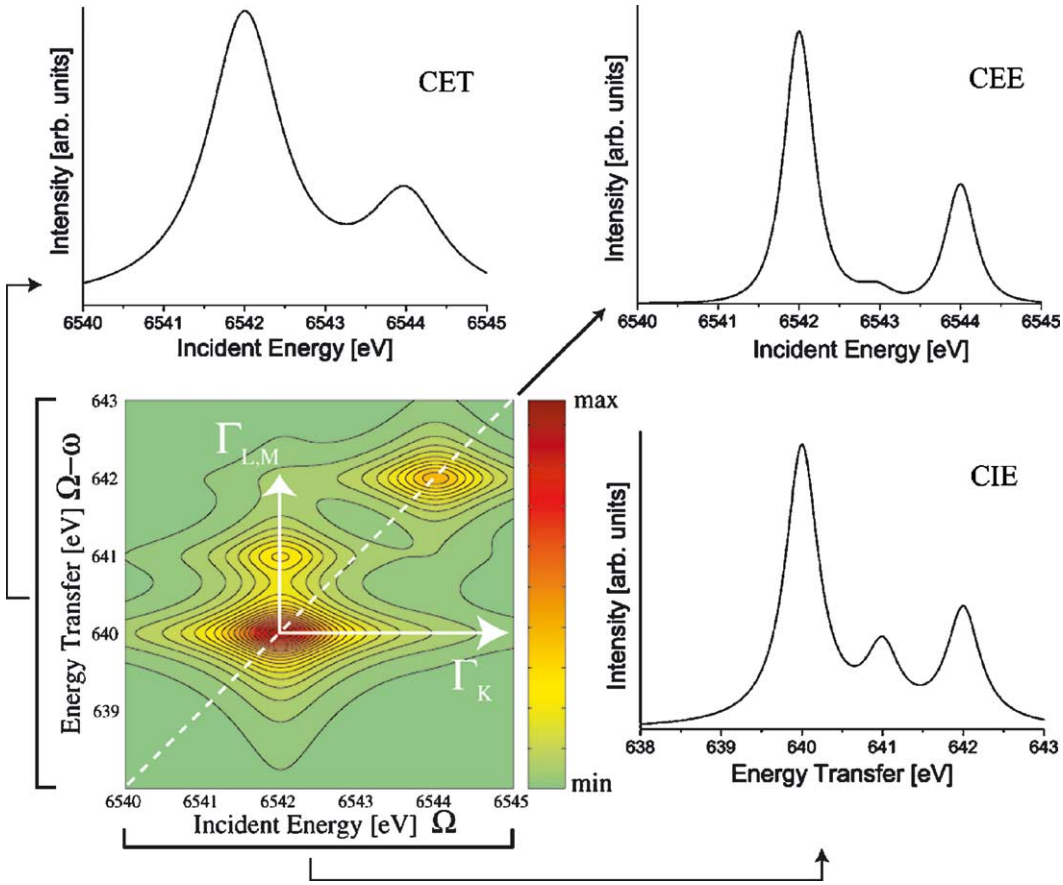

Fig. 22. Theoretical RIXS plane with three line plots. The lifetime broadenings and the diagonal cut that results in the CEE line plot are indicated in the RIXS plane. The relative spectral intensities in the RIXS plane are given in the shaded bar. The peak that lies off the diagonal corresponds to the multiplet split final state that is shown as a dotted line in Fig. 20. The brackets indicate the integration range for the CET and CIE line plots, respectively.

energy, respectively. The splitting of the two resonances can be due to either a ligand field or (3d,3d) multiplet interactions. (We neglect all many-electron transitions, such as charge transfer and shake transitions—that are not described within a single configuration multiplet theory.) A third peak occurs in the vertical or final state energy direction at the same incident energy as the first 1s resonance.

Along the vertical direction the incident energy or, equivalently, the intermediate state electron configuration is constant. As seen in Fig. 20, a scan in the vertical direction of the (Ω,Ω–ω) RIXS plane means that a $1s3d^{n+1}$ intermediate state (or Ω) is kept fixed while the final states (or Ω–ω) are varied. Such a scan shows all those final states that are reached via one particular 1s resonance. Similarly, a horizontal constant final state or constant energy transfer scan keeps a $(2,3)p^5 3d^{n+1}$ final state (or Ω–ω) fixed while the intermediate states (or Ω), i.e. the K pre-edge resonances, are scanned. It shows all those 1s resonances that decay into this particular final state. In most real systems it is not possible to separate a single electronic state because the energy splittings between different states are smaller than the lifetime broadenings. An experimental spectrum thus combines several intermediate states in constant incident energy scans and several final states in constant energy transfer scans.

The (1s, 3d) electron–electron interactions in the intermediate states are by a factor 50–100 weaker than the ((2,3)p,3d) interactions and therefore do not visibly shape the K pre-edge. A diagonal line in the maxima of the pre-edge peaks would thus represent a symmetry axis for the (Ω, Ω–ω) RIXS plane if all final state (2,3)p interactions were zero ((2,3)p spin–orbit and ((2,3)p,3d) multiplet interactions) and the lifetime broadenings assumed equal. In this case, the intermediate state 1s hole is simply replaced by a 2p or 3p hole in the final state without any consequences on the spectral shape. The (3d,3d) multiplet interactions are present in the intermediate and in the final states and thus affect the spectrum in a fashion that is symmetric to the diagonal axis.[4] However, the (2,3)p final state interactions give rise to additional peaks for each resonance

[4] We neglect that the magnitudes of the (3d,3d) Slater integrals slightly differ between the intermediate and final states. Furthermore, we neglect all weak 'off-diagonal' many electron transitions that are not described within a single configuration multiplet approach and are not due to final state interactions.

at the same incident energy shifted towards higher energy transfer and thus break the symmetry relative to the diagonal line. In the energy scheme of Fig. 20, these additional final states are indicated by the dotted line and in Fig. 22 by the off-diagonal peak. This is an important observation for the interpretation of the experimental spectra.

Fig. 22 shows three line plots. Two line plots were obtained by integrating the spectral intensity in the RIXS plane along the incident energy and the energy transfer, respectively, within certain narrow limits around the resonances. We use the acronym constant energy transfer (CET) to denote those line plots where the intensity is integrated over the energy transfer Ω–ω and plotted versus the incident energy Ω. The resulting spectrum corresponds to a constant final state scan over a certain range of final states. The lifetime broadening in such a scan arises from the 1s core hole (Γ_K). We note that such a scan becomes identical to a regular K-edge XANES scan if the integrated range extends over all final state energies.

We use constant incident energy (CIE) to denote those line plots where the intensity is integrated over the incident energy Ω and plotted versus the energy transfer Ω–ω. The resulting spectrum corresponds to a constant intermediate state scan over a certain range of intermediate states. A CIE line plot in 1s2p (1s3p) RIXS is formed by the same final state configuration as an L-edge (M-edge) absorption spectrum. The line broadening arises solely from the final state lifetime $\Gamma_{L,M}$ that is in most cases considerably smaller than the intermediate state lifetime.

It is experimentally rather elaborate to record the entire RIXS plane. Instead, one can record the intensity at constant analyzer (emission) energy ω while scanning the incident energy Ω. This corresponds to a diagonal cut through the (Ω, Ω–ω) RIXS plane (cf. Fig. 22) [151–153]. Correspondingly we denote them as constant emission energy (CEE) scans. Since the cut in the RIXS plane occurs at an angle of 45°, the scan can be projected on either the incident energy or the energy transfer axis. In the literature, the intensity is always plotted versus the incident energy and we follow this convention. Fig. 22 illustrates that the peaks in a CEE scan appear sharper than Γ_K and $\Gamma_{L,M}$ because the scan is performed in the RIXS plane at 45° with respect to the lifetime broadenings. The line broadening in a diagonal scan can be estimated from [152]:

$$\Gamma_{CEE} = \frac{1}{\sqrt{(1/\Gamma_{1s}^2) + (1/\Gamma_{L,M}^2)}} \quad (8)$$

It is important to note that such scans might differ from an actual absorption scan not only with respect to the peak broadening but also with respect to the number of peaks and the intensity ratios as we will discuss in the following. This is due to the above mentioned final state interactions as was pointed out by e.g. Carra et al. [154].

Comparison between the CEE and the CET line plot in Fig. 22 clearly shows the line sharpening effect in the CEE scan. In our simple theoretical model, the CET plot identifies with an absorption scan with two 1s–3d resonances at 6542 and 6544 eV. The CIE plot shows a third peak at 641 eV energy transfer that arises from a final state interaction. This third peak also appears weakly in the CEE plot at 6543 eV incident energy and we could be led to assume a third 1s–3d resonance that is revealed by the line sharpening effect. But a look at the whole RIXS plane tells us that the intensity arises from the tail of the lifetime broadening Γ_K of the feature at 641 eV energy transfer and thus indicates a final state interaction and not an additional 1s–3d resonance. This example demonstrates the potential pitfalls of CEE scans and explains why it is useful to record the entire RIXS plane. Keeping that in mind, we show below that CEE scans can nevertheless yield valuable spectra if the full RIXS plane is not measured out of experimental considerations (e.g. quick scans for time evolution, radiation damage). We furthermore note that a CEE plot can be calculated from the Kramers–Heisenberg equation.

8.2.1. Continuum excitations

Resonant excitations appear along a diagonal line in the (Ω, Ω–ω) plane. Excitations into the continuum can be viewed as an infinite number of resonances that lie infinitely close in energy. Such a treatment of the continuum leads to the arctangent description of the K-edge [155]. Consequently, we find that the continuum excitations show as a diagonal streak in the RIXS plane (Fig. 23 left). Like for isolated resonances, the lifetime broadenings of the continuum excitations stretch horizontally and vertically in the incident energy and energy transfer direction, respectively.

The Raman–Stokes line shift describes how the maximum of the peak intensity moves in the RIXS plane [156]. We see in Fig. 23 left that for low incident energies the

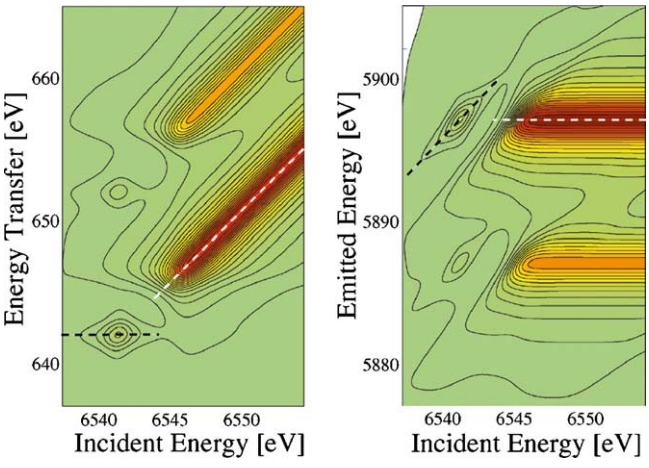

Fig. 23. Theoretical RIXS planes for a model system with one resonance and two final states. The final states are split into $2p_{3/2}$ and $2p_{1/2}$ by the 2p spin–orbit interaction. A band of continuum excitations forms the main edge. The incident energy is plotted vs. the energy transfer in the left plot and vs. the emitted energy in the right plot. The dotted lines illustrate the Raman–Stokes line shift.

maximum moves parallel to the incident energy axis in the (Ω,Ω–ω) plane because of the lifetime broadening Γ_K. Towards higher incident energies the intensity from continuum excitations begins to dominate and the maximum moves along a diagonal line. The Raman–Stokes line shift is in the literature often shown in a (Ω, ω) plot (Fig. 23 right) [157].

8.2.2. K pre-edge detection and the line sharpening effect

We see in Fig. 23 that the peak at smaller energy transfer ($2p_{3/2}$ final state) appears to sit on a lower background than the peak at larger energy transfer ($2p_{1/2}$ final state). This can also be observed in the experimental 1s2p RIXS spectrum of NiF_2 (cf. Fig. 25). The background arises from the 1s lifetime broadening of the resonant 1snp ($n = 4, 5, \ldots$) and continuum excitations that give rise to the K main edge and stretch at 45° in the (Ω, Ω–ω) plane. The background decreases towards lower energy transfer and becomes negligible in the range of the $2p_{3/2}$ feature. Since the 1s lifetime broadening extends in the horizontal direction, the $2p_{3/2}$ feature is hardly affected by the background from higher excitations. A CEE scan that only includes the $2p_{3/2}$ feature thus shows much better resolved pre-edge features than a conventional absorption scan that integrates over all final states. We can furthermore observe an additional sharpening effect as described in Eq. 8.

We show four different line plots of the NiF_2 1s–3d resonance in Fig. 24. The CEE and CET line plots were obtained from the experimental 1s2p RIXS plane as shown in Fig. 25. In the two CEE scans ((b) and (c)) the resonance is better isolated from the main edge than in the absorption spectrum. The peak in the CEE scan with 1 eV analyzer energy bandwidth is sharper and shows a slight asymmetry due to the 2p final state interactions. The spectrum (c) was obtained by convoluting the experimental spectrum in Fig. 25 with a 5 eV FWHM Gaussian function along the energy transfer direction. No asymmetry is visible in the 5 eV CEE scan because the analyzer bandwidth integrates over all $2p_{3/2}$ final states. It is remarkable that even a 5 eV analyzer energy bandwidth results in a better resolved K pre-edge peak. We show this spectrum as a suggestion for future experimental designs where some energy resolution of the fluorescence spectrometer could be sacrificed in favor of a larger solid angle.

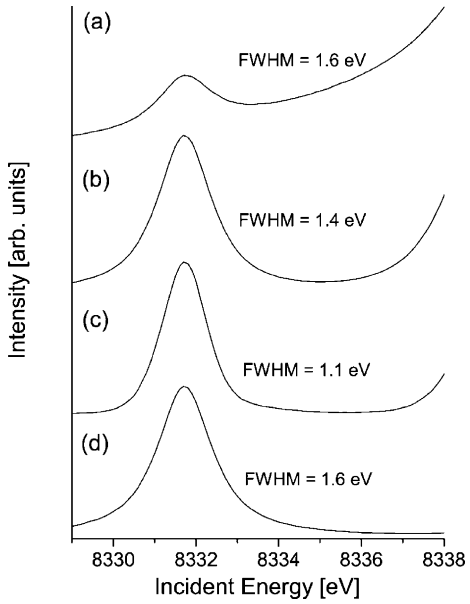

Fig. 24. Experimental spectra of the 1s–3d resonance in NiF_2: (a) K absorption pre-edge; (b) CEE line plot with 5 eV emission analyser bandwidth; (c) CEE line plot with 1 eV emission analyser bandwidth; (d) CET line plot integrated over $2p_{3/2}$ final states. The Full Width at Half Maximum (FWHM) of the 1s–3d resonance peak is given.

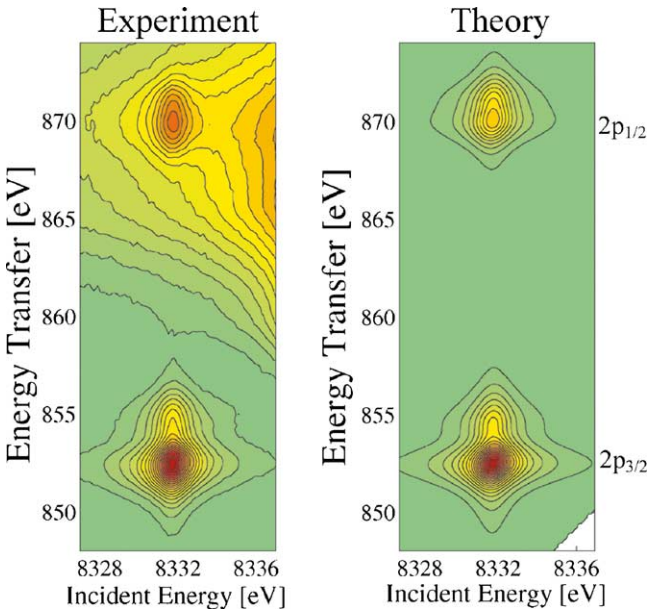

Fig. 25. 1s2p RIXS plane of NiF_2 (left) with ligand field multiplet calculations (right) for a Ni(II) high-spin complex in octahedral geometry with 10 Dq = 1.5 eV. The applied lifetime broadenings are $\Gamma_K = 1.4$ eV and $\Gamma_L = 0.7$ eV for the intermediate and the final state, respectively, as well as 0.7 eV and 1.0 eV for the instrumental energy broadening of the incident and the emitted light, respectively.

The main edge is removed in the CET scan (spectrum (d)) integrated over all $2p_{3/2}$ final states. The plot was extracted from the RIXS plane in NiF_2. This is the preferred plot to display the lowest 1s resonances because it can be directly compared to calculation of the absorption spectrum that only includes the lowest 1s excitations (cf. Fig. 24(a) and (d)).

8.2.3. Fluorescence detected absorption

To find a relation between an absorption scan and fluorescence detection using a crystal analyzer we use the following simple equation:

$$\sigma_a = \sum_i \sigma_i \tag{9}$$

The absorption cross section σ_a is expanded into a sum of partial cross sections σ_i. The index i runs over all final states that can be reached from the 1s excited states of the

absorption spectrum, i.e. it runs over all decay channels of the excited states. A CET scan for exactly one final state, i.e. if the electronic states could be perfectly separated, would give σ_i. One partial cross section σ_i is unlikely to be proportional to the absorption cross section, i.e. to have the same spectral shape. However, it is possible to select a limited sum of decay channels in order to obtain the absorption spectral shape. This is done in conventional fluorescence detected absorption spectroscopy when the intensity of the Kα lines is recorded using, for example, a solid state detector. In this technique, CEE scans are recorded with the intensity integrated over a broad band of emission energies whose width depends on the detector resolution and is much larger than any Kα spectral feature. Even though such scans traverse diagonally through the (Ω, Ω–ω) plane they still correspond to a sum of constant final state cross sections because there is basically no spectral intensity from $2p^5$ final states outside of the diagonal band that is selected by the solid state detector (cf. Fig. 23).

A considerable number of decay channels, e.g. all Kβ lines and all non-radiative transitions, are neglected in this technique. But it was shown that the Kα intensity change is proportional to the absorption cross section [158]. If we restrict the decay channels to the $K\alpha_1$ ($2p_{3/2}$ or 'L_3') line it is reasonable to assume that the resulting spectrum deviates only slightly from an absorption scan.

8.3. Experimental results

The spectra we show in the following were taken at the BioCAT undulator beamline 18ID at the Advanced Photon Source with instrumental energy broadenings of 0.7–1.2 eV for both, the incident and the emitted beam. The data acquisition time for a full RIXS plane of a concentrated sample was 2–4 h with a peak count rate of ~30 000 counts/s. This limit is set by the range of the detector linearity. Filters were used to attenuate the incident beam in order to prevent detector saturation and/or radiation damage.

8.3.1. Nickel

Nickel in various chemical environments has been comprehensively studied in soft X-ray L-edge absorption spectroscopy [159–161]. The computational effort for multiplet calculations is comparatively small and it serves as a nice example to demonstrate important aspects of ligand field multiplet theory. We therefore begin our overview of RIXS spectra with 1s2p RIXS on Ni and show in Fig. 25 the measured and calculated 1s2p RIXS plane of NiF_2 at the K pre-edge. The spectrum is divided into the $2p_{3/2}$ ('L_3') and $2p_{1/2}$ ('L_2') features at low and high-energy transfer, respectively, split by the 2p spin–orbit interaction. We note that the strict division into J=1/2 and J=3/2 is not entirely correct. Configuration interaction and angular momentum recoupling mix the states and the two spectral features cannot assigned exclusively to two different total angular momenta [65].

Fig. 26 illustrates the properties of 1s2p RIXS for Ni in various spin and oxidation states [59]. We focus on the pre-edge excitation region that involves the lowest unoccupied molecular orbitals and on $2p_{3/2}$ final states (L_3-edge). The weak 1s → 3d resonances are now separated from the strong dipole allowed transitions at higher energies. The Ni(I) complex has one vacant 3d orbital; accordingly we only observe one 1s → 3d resonance. For Ni(II), there is either a single vacant 3d orbital (low-spin) or a pair of nearly degenerate 3d orbitals (high-spin); again, we see only a single 1s → 3d resonance. In contrast, two 1s → 3d resonances are observed for the Ni(III) complex. This is consistent with at least some $3d^7$ character in the ground state configuration. Here, the Ni site has approximately tetragonal symmetry, and the low-spin ($S = 1/2$) configuration yields one unoccupied $3d_{x^2-y^2}$ orbital and a half-filled $3d_{xy}$ orbital.

We extracted CIE and CET line plots from the RIXS planes centered at the energies as indicated in Fig. 26 by the horizontal and vertical lines. The spectra are compared to K-edge and L-edge conventional absorption scans in Fig. 27. The shifts of the 1s → 3d resonances with oxidation state are clearly visible in the CET scans. No shift appears between the Ni(II) high-spin and low-spin complexes. The two strong 1s–3d resonances in the Ni(III) complex are nearly invisible in the conventional absorption spectrum. This demonstrates the potential of RIXS spectroscopy; it enables to separate out the lowest unoccupied molecular orbitals localized on a metal ion using bulk sensitive hard X-rays.

The CIE scans show more spectral features than the CET spectra. The additional peaks are due partly to multiplet ef-

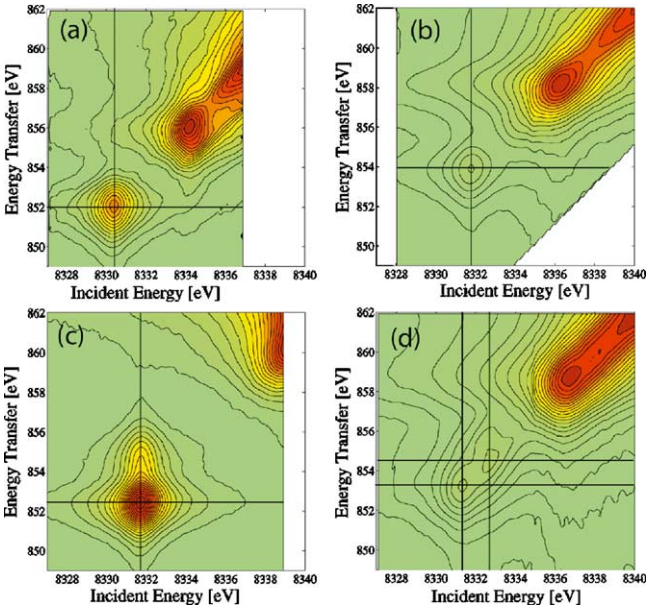

Fig. 26. Contour plots for Ni coordination complexes: (a) Ni(I) in [PhTt^{tBu}]NiCO, Ni(II) (b) low-spin (ls) in $(Ph_4As)_2Ni(S_2C_2(CF_3)_2)_2$, Ni(II) (c) high-spin (hs) in NiF_2 and (d) Ni(III) low-spin in [Ni(η^4-DEMAMPA-DCB)]$^-$. The vertical (constant incident energy) and horizontal (constant final state energy) lines correspond to the line plots shown in Fig. 27.

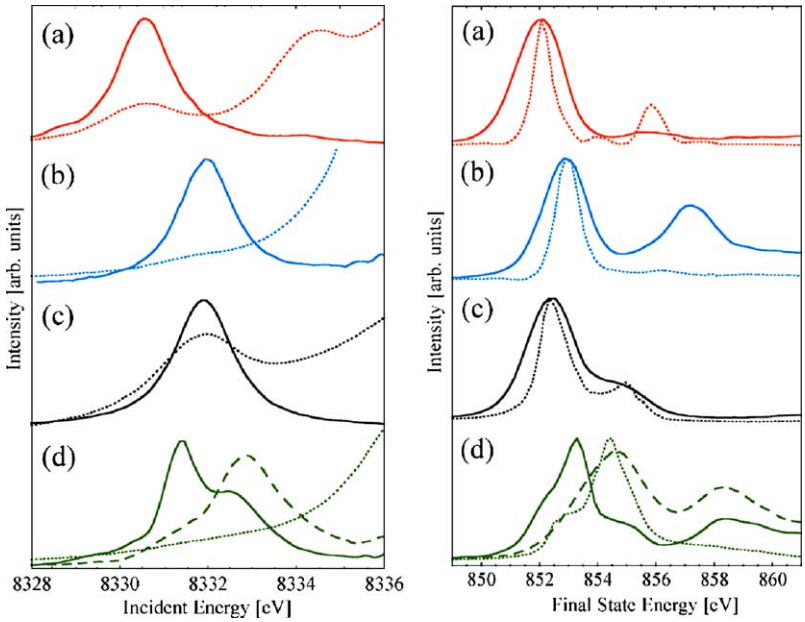

Fig. 27. Conventional absorption spectra (dotted lines) compared to RIXS line plots (solid/dashed lines) as indicated in Fig. 26 for the four Ni coordination complexes. Left panel: K pre-edge absorption spectra and CET line plots; Right panel: L_3-edge absorption spectra and CIE line plots. (reprinted with permission from ref. [59]).

fects and partly to tails of resonances at higher incident energies. It is important to always interpret the spectra with respect to the full RIXS plane. In the following, we discuss the $2p_{3/2}$ ('L_3') structure below 855.5 eV final state energy. In this case, exciting the 1s → 3d intermediate resonance of the Ni(I) complex yields final states with a $2p^5 3d^{10}$ configuration. The CIE spectrum does not show any splitting because of the filled 3d shell. Within the experimental resolution, a symmetrical peak is also observed for low-spin Ni(II). In contrast, the high-spin Ni(II) and low-spin Ni(III) L_3 CIE spectra exhibit asymmetries due to multiplet structure. These features arise from (2p,3d) and (3d,3d) Coulomb and exchange interactions. Additional structures arise from orbital energy splittings in the case of Ni(III). Multiplet splitting yields information on the valence and spin state of the metal center, and various L-edge studies have used these features to characterize metal centers [161]. Specifically, in L-edge spectroscopy, the high-energy shoulder in the L_3 line has been used as a diagnostic of high-spin Ni(II) in metalloproteins, while a low energy peak ascribed to Ni(III) has been used to characterize Ni oxides [160,162]. The high-energy shoulder in NiF_2 is well reproduced in the multiplet calculations shown in Fig. 25.

As an application of RIXS spectroscopy in biocatalysis we show results from 1s2p RIXS in Ni containing enzymes. [NiFe] hydrogenases catalyze the oxidation and formation of molecular hydrogen ($H_2 \rightarrow 2H^+ + 2e^-$) [163–166]. They contain a single [NiFe] active site and an understanding of the Ni spin and oxidation state is crucial in order to develop mechanisms for the catalytic cycles. Fig. 28 shows the CET line plots extracted from the Ni 1s2p RIXS plane recorded on the [NiFe] hydrogenase from *Desulfovibirio gigas* [167]. The data were recorded on the protein in the oxidized and in the dithionite-reduced state. The shift of the pre-edge peak to lower incident energies indicates the reduction of Ni upon treatment with dithionite.

The soluble hydrogenase (SH) of *Ralstonia eutropha* is a special hydrogenase because it is one of very few oxygen-tolerant hydrogenases; it can oxidize H_2 under aerobic conditions [168]. A mutant of the soluble hydrogenase that shows a strongly increased sensitivity to oxygen in activity measurements can be prepared by deletion of the hypX gene [169]. Fig. 29 shows the results for soluble hydrogenase purified from the hypX-positive ($SH(HypX^+)$) and hypX-negative ($SH(HypX^-)$) strain. The active site of

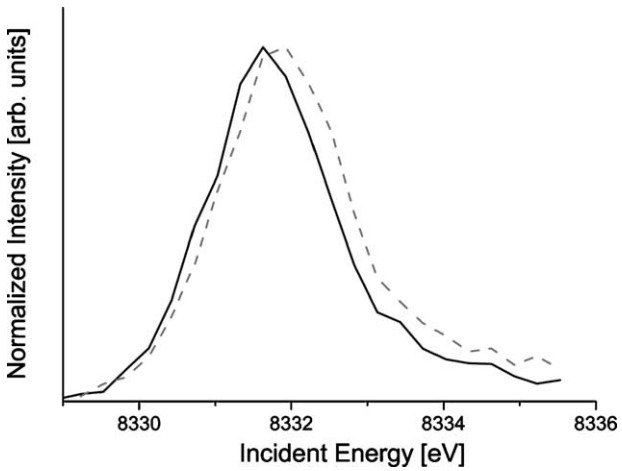

Fig. 28. CET plots for *D. gigas* hydrogenase in the oxidized form (dashed line) and reduced with dithionite (solid line).

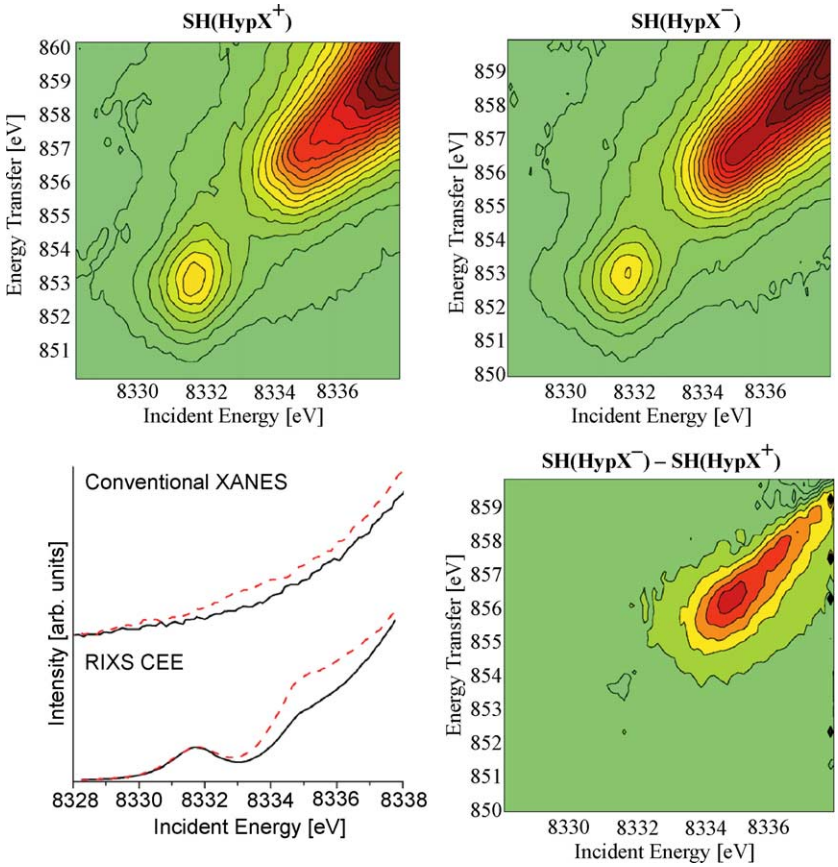

Fig. 29. Top panels: Ni 1s2p RIXS planes for two forms of the hydrogenase from *Ralstonia eutropha*. Bottom panels, left: Conventional absorption scans and CEE plots obtained from the RIXS planes (solid line: SH(HypX$^+$); dashed line: SH(HypX$^-$)); The emission energy was integrated over 4 eV to obtain the CEE plots; right: difference between two the RIXS planes; the spectra were normalized before subtraction to have equal pre-edge spectral areas.

SH(HypX$^+$) contains four cyanide ligands. Based on FTIR studies it was proposed that three cyanide groups are bound to Fe and one to Ni. Only three cyanide groups are found in the mutant SH(HypX$^-$).

The RIXS spectra show that the spectral shape of the pre-edge feature remains unchanged between the two forms. Since the pre-edge peak arises from excitations into orbitals that are mainly localized on the Ni we conclude from this result that Ni does not change its spin or oxidation state. However, a resonance at higher incident energy (8335 eV) gains in intensity in the SH(HypX$^-$) form. In this case the excited electron occupies a more delocalized orbital and the increase in intensity might reflect a change of a Ni ligand. It was proposed, that a Ni CN$^-$ ligand is replaced by an OH$^-$ ligand between the SH(HypX$^+$) and SH(HypX$^-$) [170]. This would be in agreement with this qualitative interpretation of the RIXS results. For a better understanding of the RIXS results one would need to perform a study on a series of model compounds in combination with density–functional calculations. Unfortunately, it is not possible to perform Fe RIXS experiments on the same sample because Fe also occurs in several other sites of the protein.

The comparison in Fig. 29 between the conventional absorption spectra and the CEE scan shows that RIXS enables to draw much more detailed conclusions; the absorption spectra do not reveal any well defined resonance.

8.3.2. Iron

In the following we discuss 1s3p RIXS on Fe(II) and Fe(III) in octahedral environments. A high-spin Fe(III) complex has a $t_{2g}^3e_g^2$ ($^6A_{1g}$) ground state configuration. The only 1s excited states that can be reached from the ground state are the $[1s]t_{2g}^4e_g^2$ ($^5T_2$) and $[1s]t_{2g}^3e_g^3$ (^5E) state and the K pre-edge splitting therefore directly reflects the ligand field parameter 10Dq [125].

Fig. 30 shows the 1s3p RIXS plane of α-Fe_2O_3 (hematite). The two ligand field split pre-edge peaks are visible and we obtain 10Dq = 1.4 eV. We note that the additional 3d electron in the RIXS intermediate state yields a 10Dq value that is only about 80% of those obtained from optical data [171,172]. The second resonance shows a tail towards higher final state energies indicating multiplet interactions in the $3p^5$ final states.

The 1s–3d excitation spectrum in high-spin Fe(II) $Fe_{0.05}Mg_{0.95}O$ has a slightly more complex structure. The $[1s]t_{2g}^5e_g^2$ excited state can only form a $^4T_1$ symmetry state at lowest excitation energies while the $[1s]t_{2g}^4e_g^3$ excited state gives rise to $^4T_2$ and $^4T_1$ terms [125]. The latter two states

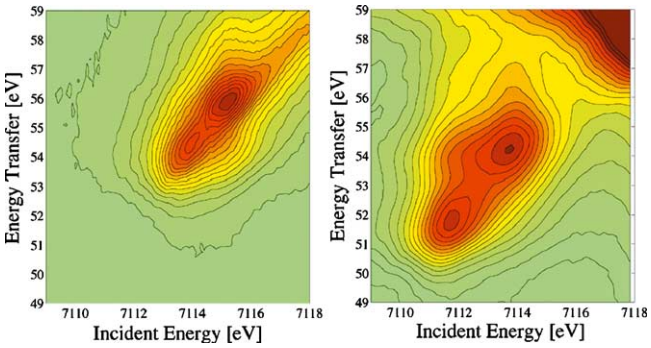

Fig. 30. 1s3p RIXS planes of Fe_2O_3 (left) and $Fe_{0.05}Mg_{0.95}O$ (right).

are split by (3d,3d) multiplet interactions with the $^4T_1$ symmetry at highest excitation energies. (We neglect spin–orbit interactions.) The separation of the two main peaks therefore does not directly reflect the ligand field splitting. We observe a pronounced shoulder towards higher final state energies at the second resonance and an intense structure between the two main peaks towards higher energy transfer. This feature is best fit with a strong multiplet splitting of the $^4T_2$ 1s resonance in the $3p^5$ final state. The additional information in the energy transfer direction will help to validate the assignment of the pre-edge features and thus to deduce the magnitudes of electron–electron interactions and ligand field splittings. Caliebe et al. performed 1s2p RIXS on hematite and showed that ligand field multiplet calculations can reproduce their observed spectral shapes [143].

The spectra in Fig. 30 show furthermore a pre-edge shift towards lower incident energies with decreasing oxidation state. Wilke et al. carried out an extensive study of the Fe pre-edge features in minerals [124]. They also determined the pre-edge intensity relative to the edge jump and found that both parameters— pre-edge position and relative intensity— are largely uncorrelated and indicative of the oxidation state and local symmetry, respectively. The experimental error in their study is mainly due to the fitting procedure of the main edge to extract the pre-edge spectral features. The pre-edge separation in RIXS spectroscopy will allow for a more accurate determination of the parameters and thus give the possibility to validate their findings.

8.3.3. Manganese

The splitting between the pre-edge and the main edge decreases towards the early transition metal complexes and it becomes more difficult to extract the pre-edge spectral features with the correct relative spectral intensities also in the RIXS spectra. In conventional absorption spectroscopy the main edge can be subtracted by assuming a arctangent shape or simply by applying a cubic spline. The RIXS plane gives the opportunity for a more sophisticated edge subtraction by fitting all CET line plots that form the RIXS plane to peak profiles. The fitted peaks that are assigned to main edge excitations then form a plane themselves that can be subtracted from the experimental RIXS plane. In Fig. 31 an example for 1s2p RIXS on MnO is shown. After edge subtraction the multiplet shoulder in the energy transfer direction of the $2p_{3/2}$ final states becomes visible. Ligand field multiplet calculations (10Dq = 1.1 eV) reproduce the spectral shape of the difference spectrum.

Fig. 32 shows the $2p_{3/2}$ final states in the 1s2p RIXS planes of MnO and $Mn(acac)_2(H_2O)_2$. The MnO spectrum appears broader than the molecular Mn(II) compound. The extracted line plots are shown in Fig. 33 with Voigt functions fitted to the CEE and CET plots. CIE and CET line plots were integrated over the energy range shown in the contour plots of Fig. 32. The splitting directly gives the 10Dq value like in the ferric O_h complexes. We obtain for 10Dq 1.1 eV for MnO and 0.7 eV for $Mn(acac)_2(H_2O)_2$ in the 1s excited states. The CIE plots show the final state multiplet splitting as a shoulder on the high energy transfer side. Soft X-ray

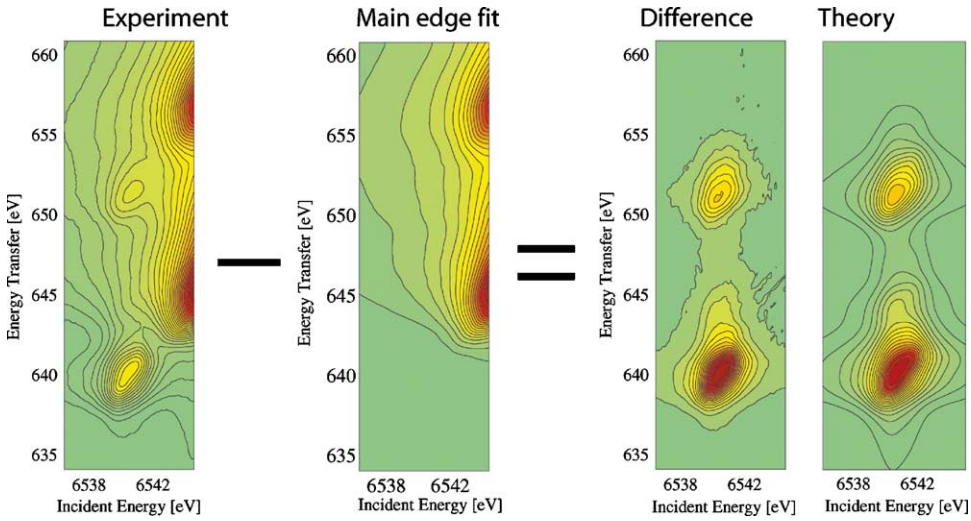

Fig. 31. 1s2p RIXS plane of MnO. A fit of the main edge was performed and subtracted from the experimental spectrum. The difference spectrum is satisfactorily reproduced in the calculated spectrum.

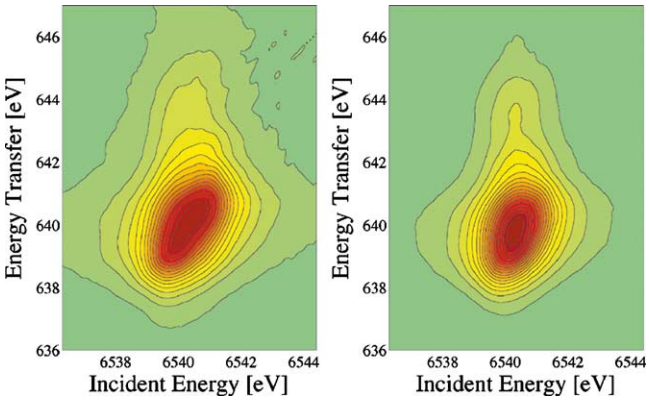

Fig. 32. $2p_{3/2}$ final states in the 1s2p RIXS planes of MnO (left) and $MnII(acac)_2(H_2O)_2$ (right). The main edge was subtracted in both cases.

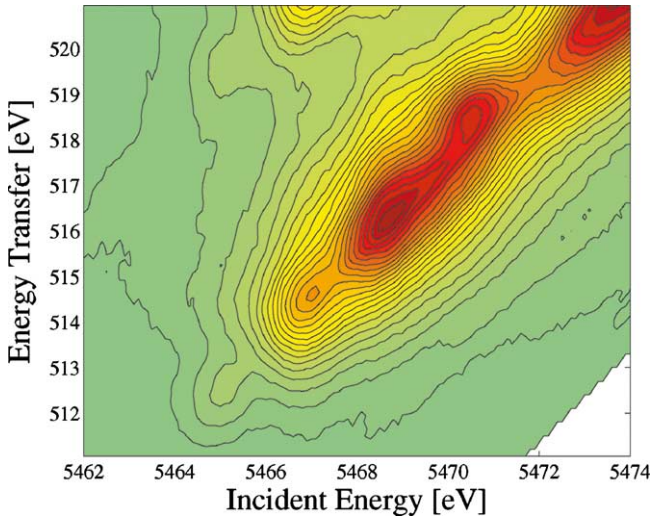

Fig. 34. $2p_{3/2}$ final states in the 1s2p RIXS plane of VF_4.

L-edge absorption spectra show a similar spectral shape for high-spin Mn(II) complexes [172].

Comparison between the CEE and CET line plots in Fig. 33 show in particular for MnO different spectral shapes. We mentioned before that CEE scans do not necessarily give the same relative peak intensities as an absorption scan. The final state integration area for the CET scan includes all $2p_{3/2}$ final state. It only slightly deviates from an absorption scan due to variations in the decay branching ratios to the $2p_{3/2}$ and $2p_{1/2}$ final states as well as symmetry mixing effects. Calculations of the 1s absorption should thus be compared to the CET and not the CEE scan.

8.3.4. Vanadium

As another example for the influence of multiplet interactions on the K pre-edge spectral shape we show the $2p_{3/2}$ final states in the 1s2p RIXS plane of VF_4 in Fig. 34. The spectrum shows four peaks almost equally spaced in energy spread over about 6 eV. The 1s resonances in VF_4 have the atomic final state configuration $1s3d^2$. The local symmetry is approximately tetrahedral with a Jahn–Teller distortion to remove the orbital degeneracy in the $3d^1$ ground state [173,174]. The lowest electron excitations and Jahn–Teller stabilization energies were calculated by Solomonik and Pogrebnaya [175]. The (3d,3d) splittings can be obtained from multiplet theory and we find that the spectrum represents an interplay between ligand field and multiplet splittings that are both on the order of 1.0–2.0 eV. The Jahn–Teller distortion is considerably stronger for electrons in the t_{2g} than in the e_g orbital and was calculated by Solomonik and Pogrebnaya to about 0.4 eV. The Jahn–Teller distortion could thus be responsible for the broader resonance shape at higher incident energies where the 1s electron is excited into the t_{2g} orbitals. It is negligible for the e_g orbitals (<0.1 eV).

We show the CET line plots together with multiplet calculations in Fig. 35. The spectral shape is poorly reproduced without (3d,3d) multiplet interactions while the full multiplet calculations can simulate the three strong structures. In

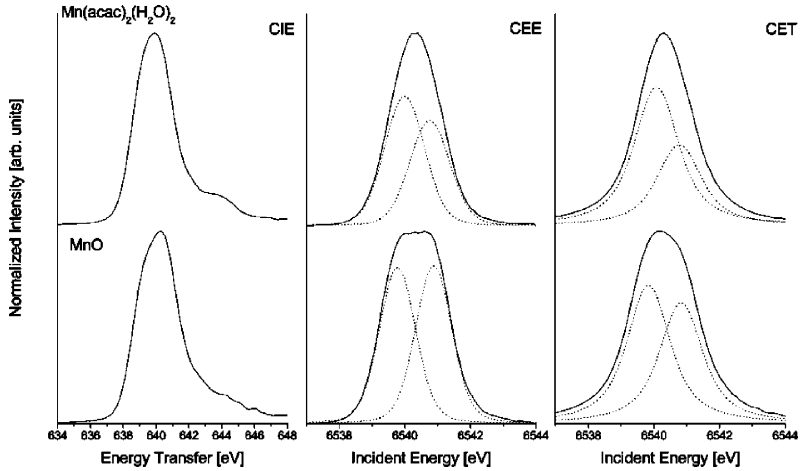

Fig. 33. Line plots and Voigt fits (dashed lines) for $Mn(acac)_2(H_2O)_2$ and MnO extracted from the 1s2p RIXS planes shown in Fig. 32. The CEE and CET plots show different line shapes and the fits yield different intensity ratios for the two resonances in both compounds.

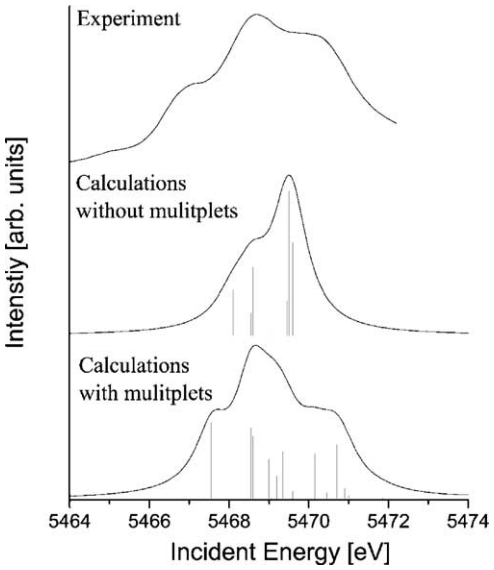

Fig. 35. Pre-edge structure in VF_4; (top) CET plot integrated between 512 and 519.5 eV energy transfer; (center) ligand field calculations (10 Dq = −1.5 eV; Ds = 0.05;Dt = −0.05 eV) with all (3d,3d) interactions set to zero; (bottom) ligand field multiplet calculations including all multiplet interactions.

order to reproduce also the weak feature at 5465 eV incident energy and the correct spectral intensities more elaborate calculations including charge transfer and dipole contributions are necessary.

8.4. Summary and outlook

In summary, we hope that this introduction to RIXS spectroscopy and short collection of examples on 3d transition metal K pre-edge RIXS has demonstrated the following important qualities of this emerging technique:

- RIXS is valuable to separate out the K absorption pre-edge features and hence to study the local electronic structure of transition metal compounds using hard X-rays.
- The energy transfer spectra are not broadened by the short 1s core hole lifetime but only by the longer final state lifetime resulting in sharper spectral features.
- Electron–electron interactions (multiplet structure) have to be included in a theoretical interpretation of the K pre-edge as well as the energy transfer spectra.
- The multiplet structure in the energy transfer spectra contains information on the electronic configuration that is complimentary to the K pre-edge. We showed examples where it is indicative of the metal ion spin state.
- By using an emission analyzer with a modest energy bandwidth of a few eV and recording the $2p_{3/2}$ ($K\alpha_1$) CEE intensity the K edge spectral features can be better resolved than in conventional absorption spectroscopy.

The resolution in the spectra shown here has been limited by instrumental broadening. An improved instrumental resolution (e.g. 0.3 eV energy bandwidth for the incident X-ray monochromator and the analyzer spectrometer) can take full advantage of the narrow final state lifetime broadening. To demonstrate the gain from a reduced energy broadening we show in Fig. 36 ligand field multiplet calculations for two different instrumental broadenings. The multiplet structure is much better resolved for $\Delta E_{\text{mono}} = \Delta E_{\text{spec}} = 0.3$ eV and a more detailed analysis of the ligand field splittings and electron–electron interactions is possible.

It is furthermore desirable to achieve instrumental resolutions that give access to interatomic (super)exchange interactions as has been done in soft X-ray RIXS and resonant photoemission [176–178]. An instrumental energy bandwidth of 10–50 meV would enable to resolve the electronic states that are split by interatomic magnetic interactions in many relevant systems, e.g. perovskites that show colossal magneto resistance (CMR) [179]. However, for such studies a final state configuration of the RIXS process has to be chosen with a lifetime broadening that is smaller than the peak splitting.

We limited our discussion to 1s2p and 1s3p RIXS, i.e. energy transfers greater than 50 eV. Studies of smaller en-

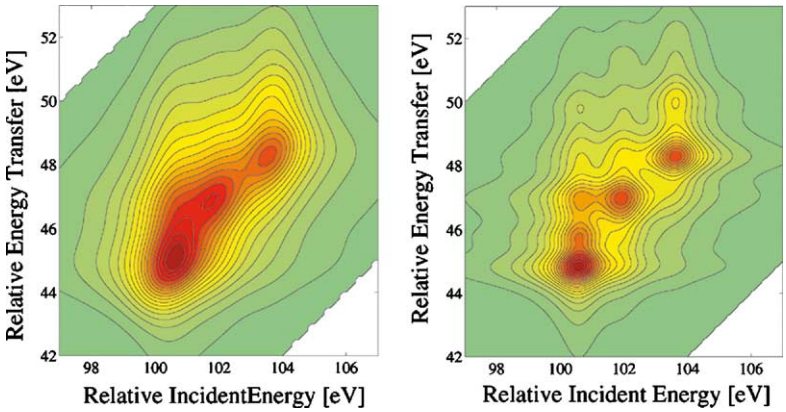

Fig. 36. Ligand field multiplet calculations for 1s2p RIXS in Fe^{2+} (10 Dq = 1.5 eV, $\Gamma_{1s} = 1.2$ eV, $\Gamma_{2p} = 0.6$ eV FWHM) with different monochromator and spectrometer energy broadenings; left: $\Delta E_{\text{mono}} = \Delta E_{\text{spec}} = 1.0$ eV; right: $\Delta E_{\text{mono}} = \Delta E_{\text{spec}} = 0.3$ eV.

ergy transfer excitations (<10 eV) that are equivalent to optical transitions have been published by several authors [180–184]. However, they mainly focused their analysis on incident energy excitations into the K main edge and for future studies it is desirable to perform detailed investigations at the K pre-edge. Furthermore, dichroism techniques can be combined with RIXS and the important field of magnetic spectroscopy is therefore possible [185]. We conclude that with the increasing impact of powerful 3rd generation storage ring X-ray sources, the future potential of RIXS spectroscopy is considerable, and applications in many disciplines of natural sciences will become possible.

9. Conclusions and outlook

We have presented spectroscopic techniques that use analysis of the X-ray emission after 1s core hole creation to obtain information on the electronic configuration and local structure in 3d transition metal compounds. They can be separated into two categories: First, experiments that do not require a tunable incident X-ray source with high resolution, and second, those who do. The first category is presented in Chapters 5 and 7, where we showed how Kα and Kβ main lines are sensitive to the local metal ion spin state and the Kβ satellite lines probe the ligand orbitals and the metal p-density of states.

Experiments of the second category include selective EXAFS as presented in Chapter 6 and RIXS as presented in Chapter 8. Selective EXAFS is a technique that uses the chemical sensitivity of the Kβ emission combined with EXAFS to distinguish local information of one element in different chemical sites. In RIXS spectroscopy as in conventional XANES, the density of the lowest unoccupied states is probed. We showed how absorption features are better resolved in RIXS and the energy transfer spectra contain information on the electronic structure that is complementary to absorption. Selective EXAFS and K pre-edge RIXS are very recent techniques and their development has been directly tied to that of powerful new third generation storage ring facilities. Our hope is that this review will introduce their potential to many physical chemists, who profit from the burgeoning field of synchrotron radiation based research.

Finally, future bright short pulse X-ray sources, such as the proposed X-ray free electron lasers (XFEL), will allow for time-resolved experiments on a femtosecond scale. The XFEL pulses have a bandpass ($\Delta E/E$) of order 10^{-3} hence less than 10 eV at 3d transition metal K edges. X-ray emission spectroscopy, both resonant and non-resonant, will be a unique tool in such time-resolved studies. The appropriate X-ray optics based on wavelength dispersive analyzers is already under development, and we expect that high-resolution 1s core hole X-ray spectroscopy on 3d transition metals will become an even more active field in the future.

Acknowledgements

The authors thank Dr. Frank de Groot, Prof. Stephen Cramer and Prof. Bernd Sonntag for their support and helpful discussions. We thank Prof. Diem Albracht, Dr. Boris Bleijlevens and Dr. Daulat Patil for their collaboration on the [Nife] hydrogenase. We are indebted to the BioCAT staff and Sergey Stepanov for their help to set up the RIXS experiment. This work was supported by the National Institutes of Health Grants GM-44380 and GM-65440 and the DOE Office of Biological and Environmental Research. UB was supported by the Stanford Synchrotron Radiation Laboratory, Department of Energy, Office of Basic Energy Sciences contract DE-AC03-765F00515. Use of the Advanced Photon Source was supported by the U.S. Department of Energy, Basic Energy Sciences, Office of Science, under contract No. W-31-109-ENG-38. BioCAT is a National Institutes of Health-supported Research Center RR-08630. The National Synchrotron Light Source and the Stanford Synchrotron Radiation Laboratory are operated by the Department of Energy, Office of Basic Energy Sciences.

References

[1] B.L. Henke, E.M. Gullikson, J.C. Davis, Atom Data Nucl. Data 54 (1993) 181.
[2] D.C. Koningsberger, R. Prins (Eds.), X-ray Absorption: Principles, Applications, Techniques of EXAFS, SEXAFS, and XANES, vol. 92, Wiley, New York, 1988.
[3] J.E. Penner-Hahn Coord, Chem. Rev. 192 (1999) 1101.
[4] B.K. Teo, D.C. Joy (Eds.), EXAFS Spectroscopy. Techniques and Application, Plenum Press, New York, 1981.
[5] D.E. Sayers, E.A. Stern, F.W. Lytle, Phys. Rev. Lett. 27 (1971) 1204.
[6] J. Goulon, C. Goulon-Ginet, R. Cortes, J.M. Dubois, J. Phys. Paris 43 (1982) 539.
[7] V.K. Yachandra, Biochem. Spectrosc. 246 (1995) 638.
[8] H. Modrow, S. Bucher, J.J. Rehr, A.L. Ankudinov, Phys. Rev. B 67 (2003) art. no. 035123.
[9] C.R. Natoli, M. Benfatto, S. Della Longa, K. Hatada, J. Syn. Rad. 10 (2003) 26.
[10] J.J. Rehr, R.C. Albers, Rev. Mod. Phys. 72 (2000) 621.
[11] A.L. Ankudinov, A. Nesvishskii, J.J. Rehr, in: Proceedings of the AIP Conference on Theory and Computation for Synchrotron Radiation Spectroscopy, Frascati, Italy, USA, 2000, pp. 105–109.
[12] B.H. Bransden, C.J. Joachain, Physics of atoms and molecules Longman Scientific & Technical, Essex, 1983.
[13] C. Cohen-Tannoudji, B. Diu, F. Laloë, Quantum mechanics, Wiley, New York, 1977.
[14] M. Weissbluth, Atoms and Molecules, Plenum Press, New York, 1978.
[15] R.D. Cowan, The Theory of Atomic Structure and Spectra, University of California Press, Berkeley, 1981.
[16] M. Nakazawa, K. Fukui, H. Ogasawara, A. Kotani, C.F. Hague, Phys. Rev. B 66 (2002) art. no 113104;
C. Dallera, M. Grioni, A. Shukla, G. Vanko, J.L. Sarrao, J.P. Rueff, D.L. Cox, Phys. Rev. Lett. 88 (2002) art. no. 196403.
[17] L. Journel, J.M. Mariot, J.P. Rueff, C.F. Hague, G. Krill, M. Nakazawa, A. Kotani, A. Rogalev, F. Wilhelm, J.P. Kappler, G. Schmerber, Phys. Rev. B 66 (2002) art. no. 045106.
[18] A. Kotani, S. Shin, Rev. Mod. Phys. 73 (2001) 203.

[19] J.B. Kortright, A.C. Thompson, in: A.C. Thompson, D. Vaughan (Eds.), X-Ray Data Booklet, second ed., Lawrence Berkeley National Laboratory, Berkeley, 2001.
[20] O. Sogut, E. Buyukkasap, H. Erdogan, Radiat. Phys. Chem. 64 (2002) 343.
[21] S. Raj, H.C. Padhi, P. Palit, D.K. Basa, M. Polasik, F. Pawlowski, Phys. Rev. B 65 (2002) art. no.-193105.
[22] K. Sakurai, H. Eba, Nucl. Instrum. Methods Phys. Res. Sect. B-Beam Interact. Mater. Atoms 199 (2003) 391.
[23] S. Friedrich, T. Funk, O. Drury, S.E. Labov, S.P. Cramer, Rev. Sci. Inst. 73 (2002) 1629.
[24] P. Glatzel, U. Bergmann, F.M.F. de Groot, S.P. Cramer, in: X-Ray and Inner-Shell Processes, American Institute of Physics, Rome, 2002, pp. 250–253.
[25] B.K. Agarwal, X-ray Spectroscopy: An Introduction, second ed., Springer, New York, 1991.
[26] A. Meisel, G. Leonhardt, R. Szargan, X-Ray Spectra and Chemical Binding, Springer, New York, 1989.
[27] P. Jonnard, G. Giorgi, C. Bonnelle, Phys. Rev. A 65 (2002) art. no.-032507.
[28] E.J. Konopinski, The Theory of Beta Radioactivity, Oxford University Press, London, 1966.
[29] P. Glatzel, Ph.D. Thesis, Hamburg University, Hamburg, 2001, http://www.sub.uni-hamburg.de/disse/570/Disse.pdf.
[30] P. Glatzel, U. Bergmann, F.M.F. de Groot, S.P. Cramer, Phys. Rev. B 64 (2001) art. no. 045109.
[31] P.S. Bagus, R. Broer, W.A. De Jong, W.C. Nieuwpoort, F. Parmigiani, L. Sangaletti, Phys. Rev. Lett. 84 (2000) 2259.
[32] P. Fulde, Electron correlations in molecules and solids, third ed., Springer, Berlin, New York, 1995.
[33] C.J. Ballhausen, Introduction to ligand field theory, McGraw-Hill, New York, 1962.
[34] J.S. Griffith, The theory of transition-metal ions, Cambridge University Press, UK, 1964.
[35] J.C. Slater, Quantum theory of atomic structure McGraw-Hill, New York, 1960.
[36] C.S. Fadley, D.A. Shirley, A.J. Freeman, P.S. Bagus, J.V. Mallow, Phys. Rev. Lett. 23 (1969) 1397.
[37] S. Hüfner, Photoelectron Spectroscopy: Principles and Applications, second ed., Springer, Berlin, New York, 1996.
[38] B. Hermsmeier, C.S. Fadley, M.O. Krause, J. Jimenez-Mier, P. Gerard, S.T. Manson, Phys. Rev. Lett. 61 (1988) 2592.
[39] K. Godehusen, T. Richter, P. Zimmermann, M. Martins, Phys. Rev. Lett. 88 (2002) art. no.-217601.
[40] B. Sonntag, P. Zimmermann, Rep. Prog. Phys. 55 (1992) 911.
[41] J. Kawai, C. Suzuki, H. Adachi, T. Konishi, Y. Gohshi, Phys. Rev. B 50 (1994) 11347.
[42] G. Zampieri, M. Abbate, F. Prado, A. Caneiro, E. Morikawa, Phys. B 320 (2002) 51.
[43] L. Hozoi, A.H. de Vries, R. Broer, Phys. Rev. B 6416 (2001) art. no. 165104.
[44] W. Kohn, L.J. Sham, Phys. Rev. 140 (1965) A1133.
[45] W. Kohn, A.D. Becke, R.G. Parr, J. Phys. Chem. 100 (1996) 12974.
[46] R.S. Mulliken, J. Chem. Phys. 23 (1955) 1833.
[47] A.E. Reed, L.A. Curtiss, F. Weinhold, Chem. Rev. 88 (1988) 899.
[48] A.L. Ankudinov, A.I. Nesvizhskii, J.J. Rehr, J. Syn. Rad. 8 (2001) 92.
[49] Y. Joly, D. Cabaret, H. Renevier, C.R. Natoli, Phys. Rev. Lett. 82 (1999) 2398.
[50] C. Suzuki, J. Kawai, H. Adachi, T. Mukoyama, Chem. Phys. 247 (1999) 453.
[51] M.A. Blokhin, X-ray spectroscopy, Hindustan Pub. Corp., Delhi, 1962.
[52] V. Stojanoff, K. Hämäläinen, D.P. Siddons, J.B. Hastings, L.E. Berman, S. Cramer, G. Smith, Rev. Sci. Inst. 63 (1992) 1125.
[53] W. Schülke, A. Kaprolat, T. Fischer, K. Höppner, F. Wohlert, Rev. Sci. Inst. 66 (1995) 2446.
[54] H.H. Johann, Z. Physik 69 (1931) 185.
[55] U. Bergmann, S.P. Cramer, in: Crystal and Multilayer Optics, SPIE, San Diego, 1998, 198–209.
[56] C.C. Kao, K. Hämäläinen, M. Krisch, D.P. Siddons, T. Oversluizen, J.B. Hastings, Rev. Sci. Inst. 66 (1995) 1699.
[57] U. Bergmann, M.M. Grush, C.R. Horne, P. DeMarois, J.E. Penner-Hahn, C.F. Yocum, D.W. Wright, C.E. Dube, W.H. Armstrong, G. Christou, H.J. Eppley, S.P. Cramer, J. Phys. Chem. B 102 (1998) 8350.
[58] J. Messinger, J.H. Robblee, U. Bergmann, C. Fernandez, P. Glatzel, H. Visser, R.M. Cinco, K.L. McFarlane, E. Bellacchio, S.A. Pizarro, S.P. Cramer, K. Sauer, M.P. Klein, V.K. Yachandra, J. Am. Chem. Soc. 123 (2001) 7804;
H. Visser, E. Anxolabehere-Mallart, U. Bergmann, P. Glatzel, J.H. Robblee, S.P. Cramer, J.J. Girerd, K. Sauer, M.P. Klein, V.K. Yachandra, J. Am. Chem. Soc. 123 (2001) 7031.
[59] P. Glatzel, U. Bergmann, W.W. Gu, H.X. Wang, S. Stepanov, B.S. Mandimutsira, C.G. Riordan, C.P. Horwitz, T. Collins, S.P. Cramer, J. Am. Chem. Soc. 124 (2002) 9668.
[60] P. Glatzel, L. Jacquamet, U. Bergmann, F.M.F. de Groot, S.P. Cramer, Inorg. Chem. 41 (2002) 3121.
[61] H. Hayashi, R. Takeda, Y. Udagawa, T. Nakamura, H. Miyagawa, H. Shoji, S. Nanao, N. Kawamura, Phys. Rev. B 68 (2003) art. no. 045122.
[62] M. Lenglet, Eur. J. Solid State Inorg. Chem. 34 (1997) 405.
[63] D.S. Urch, P.R. Wood, X-ray Spectrometry 7 (1978) 9.
[64] K. Tsutsumi, H. Nakamori, K. Ichikawa, Phys. Rev. B 13 (1976) 929.
[65] P. Wernet, B. Sonntag, M. Martins, P. Glatzel, B. Obst, P. Zimmermann, Phys. Rev. A 63 (2001) art. no. 050702.
[66] J.C. Parlebas, M.A. Khan, T. Uozumi, K. Okada, A. Kotani, J. Electron Spec. Rel. Phen. 71 (1995) 117.
[67] M. Oku, K. Wagatsuma, T. Konishi, J. Electron Spec. Rel. Phen. 99 (1999) 277.
[68] A. von dem Borne, R.L. Johnson, B. Sonntag, M. Talkenberg, A. Verweyen, P. Wernet, J. Schulz, K. Tiedtke, C. Gerth, B. Obst, P. Zimmermann, J.E. Hansen, Phys. Rev. A 62 (2000) 052703/1.
[69] G. Peng, F.M.F. Degroot, K. Hämäläinen, J.A. Moore, X. Wang, M.M. Grush, J.B. Hastings, D.P. Siddons, W.H. Armstrong, O.C. Mullins, S.P. Cramer, J. Am. Chem. Soc. 116 (1994) 2914.
[70] M. Deutsch, G. Holzer, J. Hartwig, J. Wolf, M. Fritsch, E. Forster, Phys. Rev. A 51 (1995) 283.
[71] J. Kawai, M. Takami, C. Satoko, Phys. Rev. Lett. 65 (1990) 2193.
[72] M. Taguchi, T. Uozumi, A. Kotani, J. Phys. Soc. Jpn. 66 (1997) 247.
[73] U. Bergmann, J. Bendix, P. Glatzel, H.B. Gray, S.P. Cramer, J. Chem. Phys. 116 (2002) 2011.
[74] C.R. Horne, U. Bergmann, M.M. Grush, E.J. Cairns, S.P. Cramer, J. Phys. Chem. 104 (2000) 9587.
[75] C.R. Horne, U. Bergmann, J.K. Kim, K.A. Striebel, A. Manthiram, S.P. Cramer, E.J. Cairns, J. Electrochem. Soc. 147 (2000) 395.
[76] Q. Qian, T.A. Tyson, C.C. Kao, M. Croft, S.W. Cheong, G. Popov, M. Greenblatt, Phys. Rev. B 6402 (2001) art. no.-024430.
[77] Q. Qian, T.A. Tyson, C.C. Kao, J.P. Rueff, F.M.F. deGroot, M. Croft, S.W. Cheong, M. Greenblatt, M.A. Subramanian, J. Phys. Chem. Solids 61 (2000) 457.
[78] J. Badro, V.V. Struzhkin, J.F. Shu, R.J. Hemley, H.K. Mao, C.C. Kao, J.P. Rueff, G.Y. Shen, Phys. Rev. Lett. 83 (1999) 4101.
[79] J. Badro, G. Fiquet, V.V. Struzhkin, M. Somayazulu, H.K. Mao, G. Shen, T. Le Bihan, Phys. Rev. Lett. 89 (2002) art. no.-205504.
[80] J. Badro, G. Fiquet, F. Guyot, J.P. Rueff, V.V. Struzhkin, G. Vanko, G. Monaco, Science 300 (2003) 789.
[81] J.P. Rueff, C.C. Kao, V.V. Struzhkin, J. Badro, J. Shu, R.J. Hemley, H.K. Hao, Phys. Rev. Lett. 82 (1999) 3284.
[82] J.W. Van Vleck, Phys. Rev. 45 (1934) 405.
[83] N.W. Ashcroft, N.D. Mermin, Solid state physics, Holt Rinehart and Winston, New York, 1976.

[84] J.H. Van Vleck, The Theory of Electric and Magnetic Susceptibilities, Oxford University Press, London, 1965.
[85] F.M.F. de Groot, J. Electron Spec. Rel. Phenom. 676 (1994) 529.
[86] G. van der Laan, J. Zaanen, G.A. Sawatzky, R. Karnatak, J.M. Esteva, Phys. Rev. B 33 (1986) 4253.
[87] A.E. Bocquet, T. Mizokawa, T. Saitoh, H. Namatame, A. Fujimori, Phys. Rev. B 46 (1992) 3771.
[88] D.J. Nagel, Advances in X-ray Analysis, Denver, UK Plenum, 1970, pp. 182–236.
[89] A.H. de Vries, L. Hozoi, R. Broer, P.S. Bagus, Phys. Rev. B 66 (2002) art. no.-035108.
[90] J.J. Rehr, J. Phys. Condens. Matter 15 (2003) S647.
[91] M. Taillefumier, D. Cabaret, A.M. Flank, F. Mauri, Phys. Rev. B 66 (2002) art. no.-195107.
[92] E.L. Shirley, Phys. Rev. Lett. 80 (1998) 794.
[93] E.C. Wasinger, F.M.F. de Groot, B. Hedman, K.O. Hodgson, E.I. Solomon, J. Am. Chem. Soc. 125 (2003) 12894.
[94] M.M. Grush, G. Christou, K. Hämäläinen, S.P. Cramer, J. Am. Chem. Soc. 117 (1995) 5895.
[95] Y. Izumi, H. Oyanagi, H. Nagamori, Bull. Chem. Soc. Jpn. 73 (2000) 2017.
[96] F.M.F. de Groot, Chem. Rev. 101 (2001) 1779.
[97] F.M.F. de Groot, Top. Catal. 10 (2000) 179.
[98] X. Wang, S.P. Cramer, in: Proceedings of the Ninth International Conference on X-Ray Absorption Fine Structure, Grenoble, France, 1997, pp. 361–363.
[99] G. Peng, A.X. Wang, C.R. Randall, J.A. Moore, S.P. Cramer, App. Phys. Lett. 65 (1994) 2527.
[100] K. Hämäläinen, C.C. Kao, J.B. Hastings, D.P. Siddons, L.E. Berman, V. Stojanoff, S.P. Cramer, Phys. Rev. B 46 (1992) 14274.
[101] G. Dräger, T. Kirchner, S. Bocharov, C.C. Kao, Appl. Phys. A-Mater. Sci. Process 73 (2001) 687.
[102] A.S. Koster, H. Mendel, J. Phys. Chem. Solids 31 (1970) 2523.
[103] M. Deutsch, O. Gang, K. Hämäläinen, C.C. Kao, Phys. Rev. Lett. 76 (1996) 2424.
[104] T. Mukoyama, K. Taniguchi, H. Adachi, Phys. Rev. B 41 (1990) 8118.
[105] D.S. Urch, Electron spectroscopy: Theory, Techniques, and Applications. in: C.R. Brundle, A.D. Baker, Eds., Academic Press, New York, 1979, vol. 3, pp. 1–39.
[106] U. Bergmann, C.R. Horne, T.J. Collins, J.M. Workman, S.P. Cramer, Chem. Phys. Lett. 302 (1999) 119.
[107] G. Dräger, O. Brümmer, Phys. Stat. Sol. B 124 (1984) 11.
[108] J.A. Leiro, F. Werfel, G. Dräger, Phys. Rev. B 44 (1991) 7718.
[109] G. Dräger, J.A. Leiro, Phys. Rev. B 41 (1990) 12919.
[110] A. Bianconi, J. Garcia, M. Benfatto, A. Marcelli, C.R. Natoli, M.F. Ruiz-Lopez, Phys. Rev. B 43 (1991) 6885.
[111] U. von Barth, G. Grossmann, Sol. State Commun. 32 (1979) 645.
[112] H.W. Schnopper, Phys. Rev. 131 (1963) 2558.
[113] H.W. Schnopper, Phys. Rev. 154 (1967) 118.
[114] U. Bergmann, P. Glatzel, F. deGroot, S.P. Cramer, J. Am. Chem. Soc. 121 (1999) 4926.
[115] A. Fujimori, M. Saeki, N. Kimizuka, M. Taniguchi, S. Suga, Phys. Rev. B 34 (1986) 7318.
[116] R.J. Lad, V.E. Henrich, Phys. Rev. B 39 (1989) 13478.
[117] G. Dräger, W. Czolbe, J.A. Leiro, Phys. Rev. B 45 (1992) 8283.
[118] G.B. Armen, H. Aksela, T. Åberg, S. Aksela, J. Phys. B-At. Mol. Opt. Phys. 33 (2000) R49.
[119] F. Gel'mukhanov, H. Ågren, Phys. Rep. Rev. Sec. Phys. Lett. 312 (1999) 91.
[120] E.I. Solomon, M.A. Hanson, in: E.I. Solomon, A.B.P. Lever (Eds.), Inorganic Electronic Structure and Spectroscopy, vol. 2, Wiley, New York, 1999, pp. 1–129.
[121] R.S. Czernuszewicz, T.G. Spiro, in: E.I. Solomon, A.B.P. Lever (Eds.), Inorganic Electronic Structure and Spectroscopy, vol. 1, Wiley, New York, 1999, pp. 353–441.
[122] B.N. Figgis, Introduction to Ligand Fields Interscience, New York, 1967.
[123] C.J. Ballhausen, H.B. Gray, Molecular Orbital Theory Benjamin, New York, 1964.
[124] M. Wilke, F. Farges, P.E. Petit, G.E. Brown, F. Martin, Am. Miner. 86 (2001) 714.
[125] T.E. Westre, P. Kennepohl, J.G. DeWitt, B. Hedman, K.O. Hodgson, E.I. Solomon, J. Am. Chem. Soc. 119 (1997) 6297.
[126] D. Heumann, G. Dräger, S. Bocharov, J. Phys. IV 7 (1997) 481.
[127] S. Bocharov, T. Kirchner, G. Dräger, O. Sipr, A. Simunek, Phys. Rev. B 6304 (2001) art. no.-045104.
[128] R.V. Vedrinskii, V.L. Kraizman, A.A. Novakovich, S.M. Elyafi, S. Bocharov, T. Kirchner, G. Dräger, Phys. Status Solidi B-Basic Res. 226 (2001) 203.
[129] B. Poumellec, R. Cortes, G. Tourillon, J. Berthon, Phys. Status Solidi B-Basic Res. 164 (1991) 319.
[130] T. Uozumi, K. Okada, A. Kotani, O. Durmeyer, J.P. Kappler, E. Beaurepaire, J.C. Parlebas, Europhys. Lett. 18 (1992) 85.
[131] G. Dräger, R. Frahm, G. Materlik, O. Brümmer, Phys. Status Solidi B-Basic Res. 146 (1988) 287.
[132] C. Brouder, J. Phys. Condens. Matter 2 (1990) 701.
[133] P. Carra, B.T. Thole, Rev. Mod. Phys. 66 (1994) 1509.
[134] C. Vettier, J. Electron Spec. Rel. Phen. 117 (2001) 113.
[135] S.W. Lovesey, K.S. Knight, E. Balcar, Phys. Rev. B 6405 (2001) art. no.-054405.
[136] K.D. Finkelstein, Q. Shen, S. Shastri, Phys. Rev. Lett. 69 (1992) 1612.
[137] Y. Murakami, J.P. Hill, D. Gibbs, M. Blume, I. Koyama, M. Tanaka, H. Kawata, T. Arima, Y. Tokura, K. Hirota, Y. Endoh, Phys. Rev. Lett. 81 (1998) 582.
[138] M. Takahashi, J. Igarashi, P. Fulde, J. Phys. Soc. Jap. 69 (2000) 1614.
[139] J. Danger, P. Le Fevre, H. Magnan, D. Chandesris, S. Bourgeois, J. Jupille, T. Eickhoff, W. Drube, Phys. Rev. Lett. 88 (2002) art. no.-243001.
[140] M.A. Arrio, S. Rossano, C. Brouder, L. Galoisy, G. Calas, Europhys. Lett. 51 (2000) 454.
[141] M. Taguchi, J.C. Parlebas, T. Uozumi, A. Kotani, C.C. Kao, Phys. Rev. B 61 (2000) 2553.
[142] M. Matsubara, T. Uozumi, A. Kotani, Y. Harada, S. Shin, J. Phys. Soc. Jap. 71 (2002) 347.
[143] W.A. Caliebe, C.C. Kao, J.B. Hastings, M. Taguchi, T. Uozumi, F.M.F. de Groot, Phys. Rev. B 58 (1998) 13452.
[144] J.E. Rubensson, J. Electron Spec. Rel. Phen. 110 (2000) 135.
[145] J.E. Rubensson, J. Luning, S. Eisebitt, W. Eberhardt, Appl. Phys. A-Mater. Sci. Process 65 (1997) 91.
[146] P. Salek, A. Baev, F. Gel'mukhanov, H. Ågren, Phys. Chem. Chem. Phys. 5 (2003) 1.
[147] Y.J. Ma, Phys. Rev. B 49 (1994) 5799.
[148] S. Eisebitt, W. Eberhardt, J. Electron Spec. Rel. Phen. 110 (2000) 335.
[149] F.M.F. deGroot, Phys. Rev. B 53 (1996) 7099.
[150] M.O. Krause, J.H. Oliver, J. Chem. Phys. Ref. Data 8 (1979) 329.
[151] K. Hämäläinen, D.P. Siddons, J.B. Hastings, L.E. Berman, Phys. Rev. Lett. 67 (1991) 2850.
[152] F.M.F. de Groot, M.H. Krisch, J. Vogel, Phys. Rev. B 66 (2002) art. no.-195112.
[153] H. Hayashi, Y. Udagawa, W. Caliebe, C.-C. Kao, Chem. Phys. Lett. 371 (2003) 125.
[154] P. Carra, M. Fabrizio, B.T. Thole, Phys. Rev. Lett. 74 (1995) 3700.
[155] M. Breinig, M.H. Chen, G.E. Ice, F. Parente, B. Crasemann, G.S. Brown, Phys. Rev. A 22 (1980) 520.
[156] H. Ågren, F. Gel'mukhanov, J. Electron Spec. Rel. Phen. 110 (2000) 153.
[157] P. Eisenberger, P.M. Platzmann, H. Winick, Phys. Rev. Lett. 36 (1976) 623.

[158] J. Jaclevic, J.A. Kirby, M.P. Klein, A.S. Robertson, G.S. Brown, P. Eisenberger, Sol. State Comm. 23 (1977) 679.
[159] J. van Elp, G. Peng, B.G. Searle, S. Mitra-Kirtley, Y.H. Huang, M.K. Johnson, Z.H. Zhou, M.W.W. Adams, M.J. Maroney, S.P. Cramer, J. Am. Chem. Soc. 116 (1994) 1918.
[160] H.X. Wang, C.Y. Ralston, D.S. Patil, R.M. Jones, W. Gu, M. Verhagen, M. Adams, P. Ge, C. Riordan, C.A. Marganian, P. Mascharak, J. Kovacs, C.G. Miller, T.J. Collins, S. Brooker, P.D. Croucher, K. Wang, E.I. Stiefel, S.P. Cramer, J. Am. Chem. Soc. 122 (2000) 10544.
[161] G. van der Laan, B.T. Thole, G.A. Sawatzky, M. Verdaguer, Phys. Rev. B 37 (1988) 6587.
[162] Z. Hu, G. Kaindl, S.A. Warda, D. Reinen, F.M.F. deGroot, B.G. Müller, Chem. Phys. 232 (1998) 63.
[163] J.C. Fontecilla-Camps, M. Frey, E. Garcin, C. Hatchikian, Y. Montet, C. Piras, X. Vernede, A. Volbeda, Biochemie 79 (1997) 661.
[164] J.C. Fontecilla-Camps, Struct. Bond. 91 (1998) 2.
[165] R.P. Happe, W. Roseboom, A.J. Pierik, S.P.J. Albracht, K.A. Bagley, Nature 385 (1997) 126.
[166] M. Frey, Structure and Bonding 90 (1998) 97.
[167] A. Volbeda, E. Garcia, C. Piras, A.L. deLacey, V.M. Fernandez, E.C. Hatchikian, M. Frey, J.C. FontecillaCamps, J. Am. Chem. Soc. 118 (1996) 12989.
[168] R.P. Happe, W. Roseboom, G. Egert, C.G. Friedrich, C. Massanz, B. Friedrich, S.P.J. Albracht, FEBS Lett. 466 (2000) 259.
[169] B. Bleijlevens, B.W. Faber, S.P.J. Albracht, J. Biol. Inorg. Chem. 6 (2001) 763.
[170] B. Bleijlevens, Ph.D. thesis, University of Amsterdam, Amsterdam, 2002.
[171] A.B.P. Lever, Inorganic Electronic Spectroscopy Elsevier: Amsterdam, 1984.
[172] S.P. Cramer, F.M.F. Degroot, Y. Ma, C.T. Chen, F. Sette, C.A. Kipke, D.M. Eichhorn, M.K. Chan, W.H. Armstrong, E. Libby, G. Christou, S. Brooker, V. Mckee, O.C. Mullins, J.C. Fuggle, J. Am. Chem. Soc. 113 (1991) 7937.
[173] A.C. Gossard, F.J. Di Salvo, W.E. Falconer, T.M. Rice, J.M. Voorhoeve, N. Yasuoka, Sol. State Commun. 14 (1974) 1207.
[174] S. Becker, B.G. Muller, Angew. Chem. Int. Edit. Engl. 29 (1990) 406.
[175] V.G. Solomonik, T.P. Pogrebnaya, Russ. J. Inorg. Chem. 46 (2001) 1851.
[176] F.M.F. de Groot, J. Electron Spec. Rel. Phenom. 92 (1998) 207.
[177] F.M.F. de Groot, P. Kuiper, G.A. Sawatzky, Phys. Rev. B 57 (1998) 14584.
[178] H.A. Dürr, G. vanderLaan, D. Spanke, F.U. Hillebrecht, N.B. Brookes, Phys. Rev. B 56 (1997) 8156.
[179] C. de Graaf, C. Sousa, I.D. Moreira, F. Illas, J. Phys. Chem. A 105 (2001) 11371.
[180] C.C. Kao, W.A.L. Caliebe, J.B. Hastings, J.M. Gillet, Phys. Rev. B 54 (1996) 16361.
[181] A. Shukla, J.P. Rueff, J. Badro, G. Vanko, A. Mattila, F.M.F. de Groot, F. Sette, Phys. Rev. B 67 (2003) art. no.-081101.
[182] J.P. Hill, C.C. Kao, K. Hämäläinen, S. Huotari, L.E. Berman, W.A.L. Caliebe, M. Matsubara, A. Kotani, J.L. Peng, R.L. Greene, J. Phys. Chem. Solids 61 (2000) 425.
[183] Y.J. Kim, J.P. Hill, C.A. Burns, S. Wakimoto, R.J. Birgeneau, D. Casa, T. Gog, C.T. Venkataraman, Phys. Rev. Lett. 89 (2002) art. no.-177003.
[184] P.M. Platzman, E.D. Isaacs, Phys. Rev. B 57 (1998) 11107.
[185] K. Fukui, H. Ogasawara, A. Kotani, T. Iwazumi, H. Shoji, T. Nakamura, J. Phys. Soc. Jpn. 70 (2001) 3457.